iScience

CellPress
OPEN ACCESS

Article

A dynamic actin cytoskeleton is required to prevent constitutive VDAC-dependent MAPK signalling and aberrant lipid homeostasis

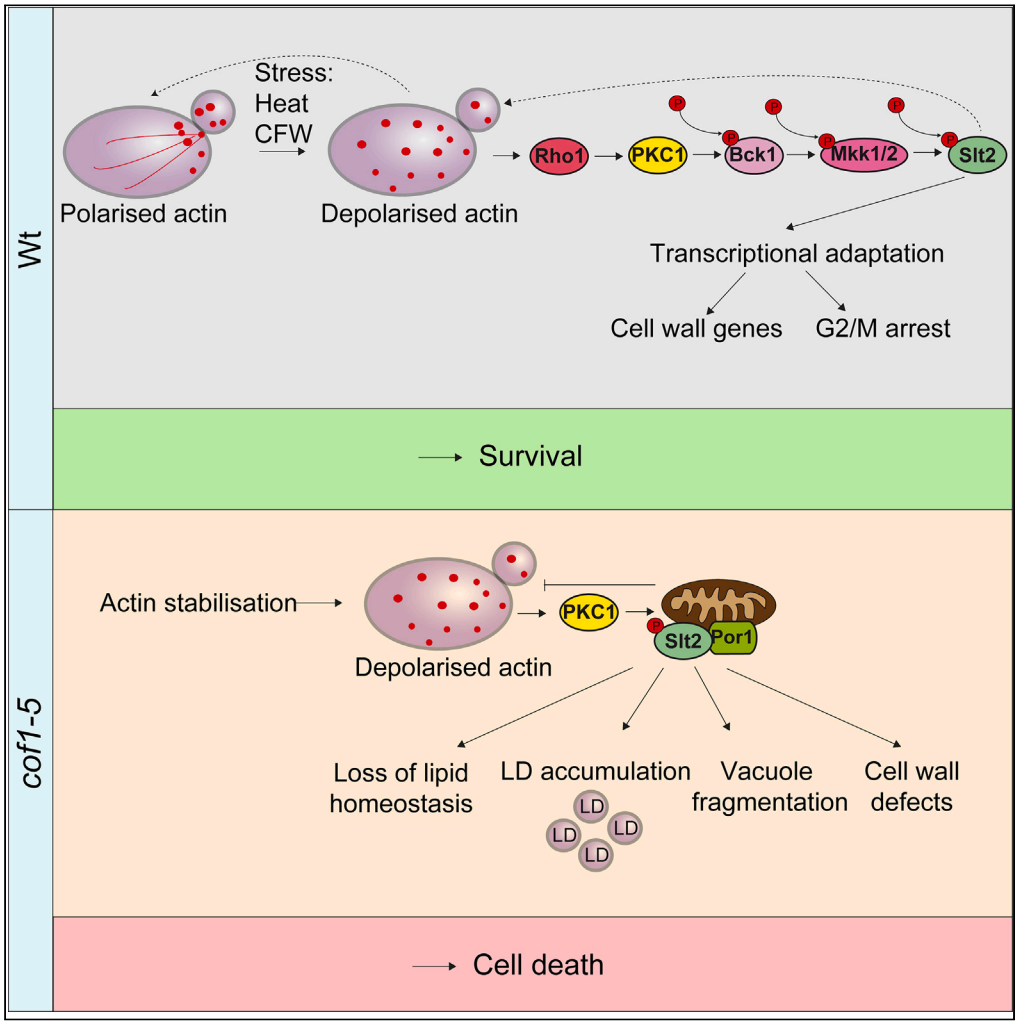

Jack Davis, Thorsten Meyer, Martin Smolnig, ..., Tobias von der Haar, Campbell W. Gourlay, Patrick Rockenfeller

Campbell.W.Gourlay@kent.ac.uk (C.W.G.)
Patrick.rockenfeller@uni-wh.de (P.R.)

Highlights

cof1-5 mutation activates CWI signaling in a VDAC-dependent manner

cof1-5 expression promotes MAPK signaling from the mitochondrial compartment

Cofilin and VDAC/Porin are important regulators of lipid homeostasis

Davis et al., iScience 26, 107539
September 15, 2023
https://doi.org/10.1016/j.isci.2023.107539

iScience

CellPress
OPEN ACCESS

Article

A dynamic actin cytoskeleton is required to prevent constitutive VDAC-dependent MAPK signalling and aberrant lipid homeostasis

Jack Davis,[1,7] Thorsten Meyer,[2,7] Martin Smolnig,[2] Daniel G.J. Smethurst,[1] Lisa Neuhaus,[2] Jonas Heyden,[2] Filomena Broeskamp,[2] Elizabeth S.M. Edrich,[1] Oskar Knittelfelder,[3,6] Dagmar Kolb,[4,5] Tobias von der Haar,[1] Campbell W. Gourlay,[1,8,9,*] and Patrick Rockenfeller[2,8,9,10,*]

SUMMARY

The dynamic nature of the actin cytoskeleton is required to coordinate many cellular processes, and a loss of its plasticity has been linked to accelerated cell aging and attenuation of adaptive response mechanisms. Cofilin is an actin-binding protein that controls actin dynamics and has been linked to mitochondrial signaling pathways that control drug resistance and cell death. Here we show that cofilin-driven chronic depolarization of the actin cytoskeleton activates cell wall integrity mitogen-activated protein kinase (MAPK) signalling and disrupts lipid homeostasis in a voltage-dependent anion channel (VDAC)-dependent manner. Expression of the *cof1-5* mutation, which reduces the dynamic nature of actin, triggers loss of cell wall integrity, vacuole fragmentation, disruption of lipid homeostasis, lipid droplet (LD) accumulation, and the promotion of cell death. The integrity of the actin cytoskeleton is therefore essential to maintain the fidelity of MAPK signaling, lipid homeostasis, and cell health in *S. cerevisiae*.

INTRODUCTION

The actin cytoskeleton participates in many cellular processes including cell and organelle architecture, endocytosis, vesicular trafficking, and organelle inheritance and communication.[1] As a result, the regulation of actin dynamics is essential and is facilitated by accessory proteins that promote rapid assembly and disassembly of filaments. Perturbations in the control of actin dynamics, instigated either through mutations in actin itself or as a result of the aberrant activity of actin regulatory proteins, have been shown to trigger cell death in a variety of cell types.[2] In many, if not all, of these cases cell death appears to be underpinned by links between the control of actin dynamics and its effects on mitochondrial function. A good example of this lies with the highly conserved actin regulatory protein cofilin. Cofilin is a member of the actin depolymerizing factor (ADF)/cofilin family of small actin-binding proteins found in all eukaryotic cells, which are essential for dynamic polymerization and depolymerization of actin.[3] Recent findings suggest that cofilin plays a role in the regulation and maintenance of homeostasis as cells adapt to environmental challenge. For example, cofilin has been shown to facilitate the control of permeabilization of the outer mitochondrial membrane, and so the initiation of apoptosis, in neutrophils at sites of infection in mammalian systems.[4] Cofilin is likely, therefore, to play a major role in innate immune and inflammatory responses. Additionally, aberrant cofilin/actin aggregates, termed ADF/cofilin rods (ACRs), which accumulate in normal aging brains and even more excessively in the hippocampus of Alzheimer's sufferers, are reported to interact with and damage mitochondria under conditions of stress.[5] Cofilin can therefore function within normal cellular responses or, if aberrant, promote disease via its interactions with mitochondria. Subtle changes to the charged surfaces of cofilin have a profound effect on the activity and quality of mitochondrial function. In yeast the regions of cofilin that are involved in controlling mitochondrial function are distinct from the actin binding and regulatory surface.[6] However, despite the mounting evidence that cofilin can control homeostasis and cell fate via mitochondrial regulation, our understanding as to how this is achieved is lacking.

Cell death can occur in many different regulated or accidental ways which are characterized by their phenotypic features.[7] Importantly, regulated cell death pathways are not limited to multicellular organisms but also occur in single-cell organisms such as *S. cerevisiae*.[8,9] The different modes and subroutines of cell

[1]Kent Fungal Group, School of Biosciences, University of Kent, Canterbury, Kent, UK

[2]Chair of Biochemistry and Molecular Medicine, Center for Biomedical Education and Research (ZBAF), University of Witten/Herdecke (UW/H), Stockumer Str. 10, 58453 Witten, Germany

[3]Max Planck Institute of Molecular Cell Biology and Genetics, 01307 Dresden, Germany

[4]Medical University of Graz, Core Facility Ultrastructure Analysis, Neue Stiftingtalstraße 6/II, 8010 Graz, Austria

[5]Gottfried Schatz Research Center for Cell Signaling, Metabolism and Aging, Division of Cell Biology, Histology and Embryology, Medical University of Graz, Neue Stiftingtalstraße 6/II, 8010 Graz, Austria

[6]Present address: Innovation Campus Berlin, Nuvisan ICB, 13353 Berlin, Germany

[7]These authors contributed equally

[8]These authors contributed equally

[9]Senior authors

[10]Lead contact

*Correspondence: Campbell.W.Gourlay@kent.ac.uk (C.W.G.), Patrick.rockenfeller@uni-wh.de (P.R.)

https://doi.org/10.1016/j.isci.2023.107539

death in yeast, which include accidental, regulated, and programmed forms of cell death, have been classified based on morphological and biochemical criteria.[10] Importantly yeast has been successfully used to study lipotoxicity/lipotoxic cell death.[11–14]

In this project we wished to gain mechanistic insight into the regulation of cofilin/actin-dependent stress signaling and mitochondrial function using the model yeast *S. cerevisiae*. In order to investigate this we made use of the well-characterized *cof1-5* mutant. In this strain two negatively charged amino acid residues are exchanged for alanine (D10A E11A). These amino acid exchanges do not interfere with actin binding *per se* but reduce cofilin's actin depolymerization efficiency, thus stabilizing the actin cytoskeleton.[15] We report that cofilin-dependent reduction in actin dynamics leads to a number of chronic defects, such as aberrant cell wall construction, vacuole fragmentation, and altered lipid metabolism that sensitizes the cells to a necrotic cell fate when they are exposed to additional stress. This "pro-death" cell state is driven by the localization and constitutive activation of protein kinase C (PKC)-controlled mitogen-activated protein kinase (MAPK) signaling at the mitochondria.

PKC activation of MAPK signaling is essential for yeast cell survival under a range of stress conditions. In addition to its canonical role in PKC/MAPK cell wall integrity (CWI), the terminal MAPK Slt2 has been shown to phosphorylate several targets involved in responses to environmental challenge. Slt2 therefore has roles in cell wall, oxidative, heat, and calcium stress, and functions within cellular processes including cell cycle control, membrane trafficking, and actin cytoskeleton organization.[16] Such perturbations to PKC/MAPK signaling are often linked to elevated cell death, highlighting its importance in cell adaption and survival.[17,18] Given the importance of the PKC/MAPK pathway to survive environmental challenge, cells have developed mechanisms to ensure that its activation is tightly controlled.[19] Here we show that a loss of actin regulation can override such controls and leads to the assembly of voltage-dependent anion channel (VDAC)/Porin1-dependent MAPK signaling at the mitochondrial compartment. Many of the phenotypes associated with *cof1-5* expression could be rescued by the deletion of *POR1*, suggesting a key and previously uncharacterized role for VDAC in MAPK signaling in yeast. In addition, the deletion of genes *LRO1* or *DGA1* that control the accumulation of triglyceride in lipid droplets (LDs) was also sufficient to prevent constitutive MAPK signaling and restore cell health in *cof1-5* mutants.

Our data suggest that the integrity of the actin cytoskeleton and the fidelity of PKC/MAPK signaling are interconnected and that their concerted action is important for cell survival. Actin stabilization promotes an MAPK signaling module that renders cells vulnerable to environmental challenge. We suggest that this adds to the growing evidence that simple eukaryotes embrace cellular states that ensure cells that cannot respond to environmental cues, such as those with corrupted actin cytoskeleton, are removed from their population.

RESULTS

cof1-5-induced actin defects and vacuole fragmentation but not mitochondrial fragmentation are VDAC dependent

In mammalian cells cofilin and its binding partner actin have been shown to interact with the mitochondrial outer membrane pore VDAC.[4,20] A primary goal of our study was to determine whether phenotypes associated with changes in actin dynamics that are linked to cofilin function are mediated via VDAC in yeast. In order to investigate this we made use of the well-characterized *cof1-5* mutant.

During cell division, cortical actin patches can be observed to polarize to the growing bud;[21–24] however, in *cof1-5* cells actin patches are observed throughout the mother and daughter.[25] We examined whether the actin depolarization phenotype observed in *cof1-5* cells was VDAC/Porin1 (Por1) dependent by staining the F-actin cytoskeleton with phalloidin-tetramethylrhodamine B-isothiocyanate (phalloidin-TRITC). Surprisingly, the deletion of *POR1* in *cof1-5* cells resulted in a full rescue of the actin depolarization phenotype (Figures 1A and 1B) and also reverted the cell size increase as observed in *cof1-5* (Figures 1A and 1C). These results suggest that the actin defect observed in dividing *cof1-5* cells is not caused by the action of cofilin on actin, but rather by either a loss of regulation that controls actin patch assembly or the induction of a cellular stress program capable of triggering actin depolarization. The rescue of actin depolarization upon deletion of *POR1* suggests an interaction between cofilin and/or actin with the mitochondrial compartment.

A further phenotype associated with *cof1-5*-expressing cells is fragmentation of the mitochondrial network.[6] As the fragmentation of mitochondria has been shown to involve F-actin and cofilin in

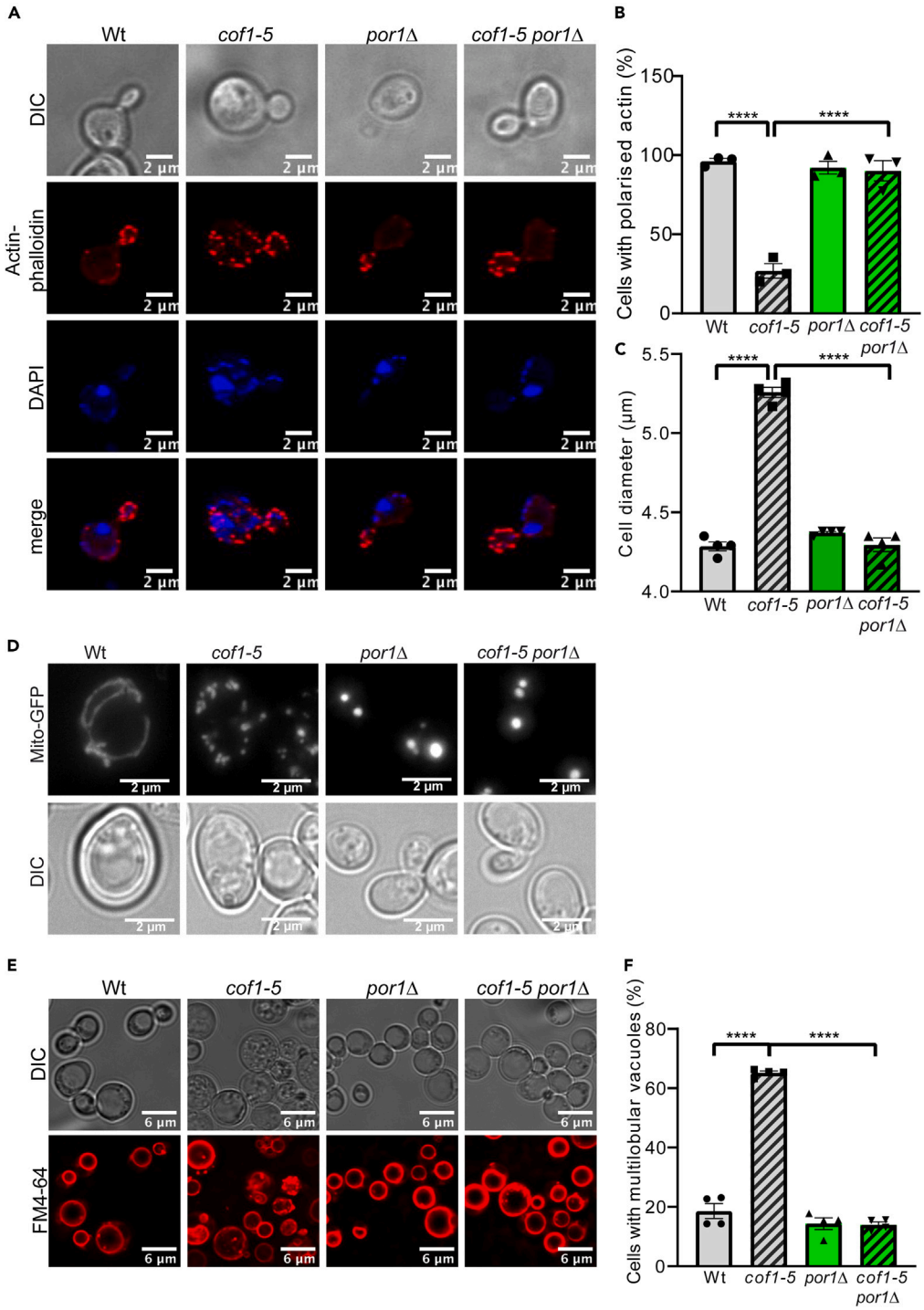

Figure 1. *cof1-5*-induced actin depolarisation but not mitochondrial fragmentation are VDAC dependent

(A and B) Actin phalloidin (red) and DAPI (blue) staining at exponential growth phase (6h) reveals depolarised actin cytoskeleton in the *cof1-5* mutant, which is rescued by additional *POR1* deletion. Representative microscopy pictures are shown in (A) and cells with polarised actin were quantified in (B).

(C) *cof1-5* cells have an increased mean cell diameter (as determined with a CASY cell counter).

(D) Fluorescence microscopy pictures at exponential growth phase of wt and *cof1-5* with and without additional *POR1* deletion expressing mitochondrial GFP from a plasmid (pVT100U-mt GFP).

Figure 1. *Continued*

(E and F) *cof1-5* mutation leads to Por1-dependent vacuole fragmentation as visualised by FM4-64 staining. Representative microscopy images are shown in (E) and a quantification of cells containing multi-lobular vacuoles is depicted in (F). Statistical significance in (B) (C) and (F) was assessed using ordinary one-way ANOVA. See also Figure S1. Error bars indicate standard error of the mean (SEM) and asterisks indicate significant differences based on p-values, *p < 0.05, **p < 0.01, ***p < 0.001, ****p < 0.0001.

mammalian cells, we considered the possibility that *POR1* deletion in *cof1-5* cells may also restore mitochondrial morphology. Deletion of *POR1* leads to the accumulation of mitochondria within a single entity (or maximally two) reminiscent of mutations in the endoplasmic reticulum (ER)-mitochondria encountering structure (ERMES), such as *mdm10*Δ, *mdm12*Δ, *mdm34*Δ, and *mmm1*Δ (Figure 1D).[26] Mitochondria of *cof1-5 por1*Δ cells also appeared as large spherical structures and identical to those of *por1*Δ (Figure 1D). As actin has also been linked to vacuole regulation, we made use of the fluorescent dye FM4-64 to examine its morphology. Interestingly, *cof1-5* cells showed an aberrant fragmented or multi-lobed vacuole morphology (Figure 1E). In *cof1-5* cells 65% of the cells had multi-lobular vacuoles as compared to only 19% in wild type (Figure 1F). Notably, knockout (KO) of *POR1* led to a full rescue of this vacuolar phenotype. Additional electron microscopy confirmed the fragmented vacuole phenotype in *cof1-5* cells (Figure S1). Altogether, these data suggest that the actin depolarization and vacuole fragmentation phenotypes observed in *cof1-5* cells are Por1 dependent, whereas mitochondrial fragmentation does not share the Por1 dependency.

The *cof1-5* mutation constitutively activates the CWI pathway in a VDAC-specific manner

In addition to changes in growth (Figure 2A), we observed that *cof1-5* mutant cells were prone to flocculation and sedimented rapidly in culture (Figure 2B). Flocculation is a natural phenomenon where cells aggregate in multicellular so-called flocs, which increases the chance of survival upon stress.[27] Flocculation involves remodeling of the cell wall and has recently been connected to CWI signaling.[28] The fungal cell wall is composed of glucans, chitin, chitosan, mannans, galactomannans, and glycoproteins.[29] Under unstressed conditions chitin is represented at only 2% of cell wall mass, which can increase up to 20% upon cell wall stress.[30] This explains the increased reactivity of yeast cells with the chitin-specific dye Calcofluor White (CFW)[31] upon cell wall stress. Using CFW staining we could indeed confirm that chitin is enriched at the mutant cell wall as compared to the wild type (Figure 2C). Examination of the cell wall ultrastructure by electron microscopy revealed that the inner cell wall of the *cof1-5* mutant appeared thicker than that in wild-type samples, whereas the electron-dense structures of the outer cell wall were slightly shorter (Figure 2D). We measured wild-type and mutant cell wall widths and calculated the means for inner and outer cell walls. Strikingly, we confirmed a substantial increase of inner cell wall width for *cof1-5* (Figure 2E), whereas the outer cell wall width was slightly reduced (Figure 2F). Moreover, we observed that these cell wall phenotypes were reversed by additional KO of *POR1*. These data suggest that VDAC is required for the maintenance of normal cell wall architecture.

Actin stabilization changes expression of genes associated with the plasma membrane compartment, MAPK signaling, and regulation of the cell wall

The *cof1-5* mutation has been shown to lead to a reduction in the dynamic nature of actin filaments.[15] However, as the deletion of *POR1* led to a rescue of the actin patch depolarization phenotype, we wished to determine whether reduced actin dynamics alone would lead to changes in the cell wall regulation. To achieve this, we made use of a well-characterized actin allele, *act1-159*, which reduces actin dynamics by slowing the release of inorganic phosphate following ATP hydrolysis within F-actin filaments.[32] The expression of *act1-159* led to a significant increase or decrease in the expression of 648 and 141 genes, respectively, during exponential growth phase (Figure 3A; Table S1). Genes that were upregulated in response to actin stabilization could be clustered within several cellular processes by Gene Ontology (Figure 3B; Table S1). The processes controlling transposition, response to pheromone, and cell wall biosynthesis, which are controlled by MAPK pathways, were enriched within the upregulated gene dataset (Figure 3B; Table S1). The changes in gene expression related to MAPK signaling in dividing *act1-159* cells were further exemplified by elevated levels of the membrane pheromone receptor *STE2* and the MAPK *FUS3*, which are normally activated by the presence of extracellular pheromone from cells of the opposite mating type. A MAPK involved in signaling in response to cell wall stresses, *SLT2* (also called *MPK1*), and the upstream mitogen-activated protein kinase kinase (MAPKK/MKK1) were also upregulated. This was accompanied by the increase in expression of several genes involved in another MAPK-controlled process, cell wall

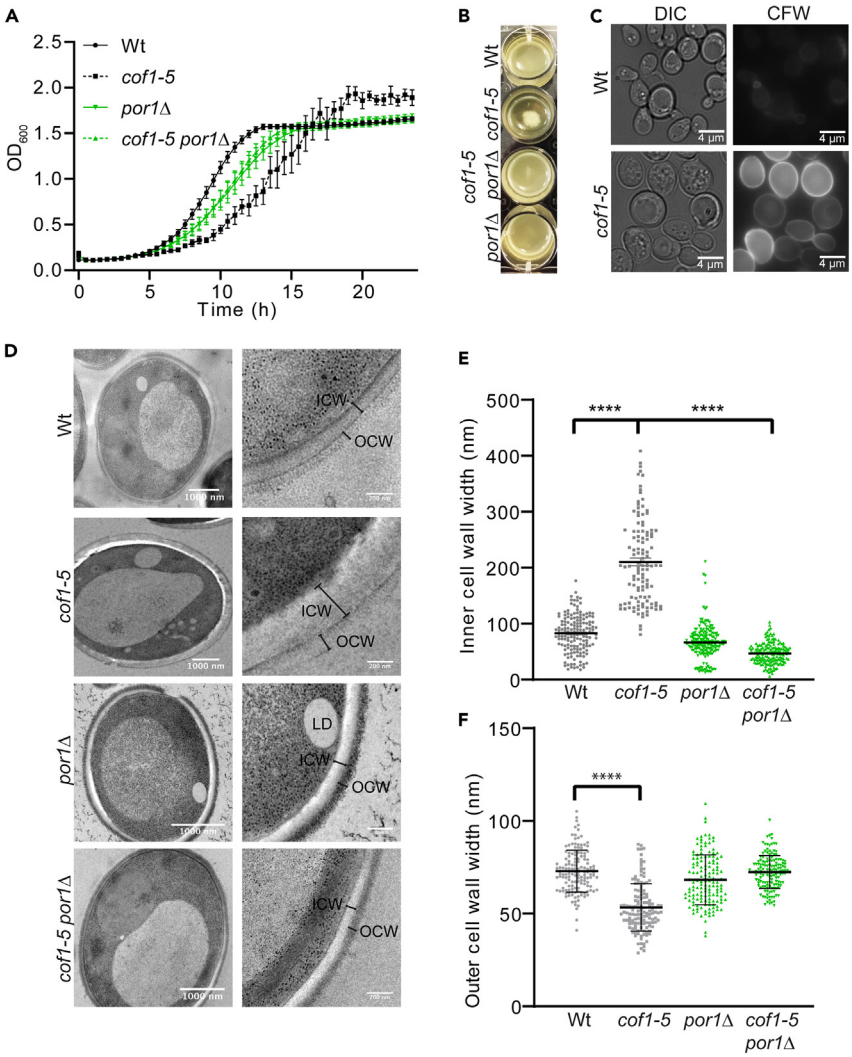

Figure 2. *cof1-5* mutation triggers growth defect, flocculation, and cell wall alterations, which depend on *POR1*

(A) Growth performance in liquid culture is reduced in *cof1-5* as compared to wild type (Wt) but is restored by additional *POR1* deletion.

(B) Cultures bearing the *cof1-5* mutation sediment quickly when shaking is stopped (flocculation phenotype). Additional *POR1* deletion prevents flocculation in *cof1-5*.

(C) Calcofluor white staining detecting chitin exposure at the cell wall confirms flocculation phenotype of *cof1-5* cells.

(D–F) The cell wall was analyzed by electron microscopy. *cof1-5* mutation is associated with a thicker inner cell wall and thinner outer cell wall. EM micrographs are shown in D and quantifications of the inner and outer cell wall are plotted in E and F, respectively. ICW, inner cell wall; OCW, outer cell wall; LD, lipid droplet. Statistical significance in (E) was assessed using Kruskal-Wallis test and in (F) Welch ANOVA was performed.

Error bars indicate standard error of the mean (SEM) and asterisks indicate significant differences based on p-values, *p < 0.05, **p < 0.01, ***p < 0.001, ****p < 0 .0001.

biogenesis (Table S1). Within the genes upregulated for cell wall regulation process were those involved in glucan, chitin, and mannan regulation as well as genes encoding several glycosylphosphatidylinositol (GPI)-anchored proteins (Table S1). To highlight the effects on cell wall we observed that *act1-159* cells exhibited a strong sensitivity to the cell wall stressor Congo Red (Figure 3C). Overall these data support the finding that actin stabilization leads to an increase in intracellular stress, a loss of MAPK regulation, which includes CWI activation, and changes in lipid biosynthesis in a manner akin to that observed in *cof1-5*-expressing cells.

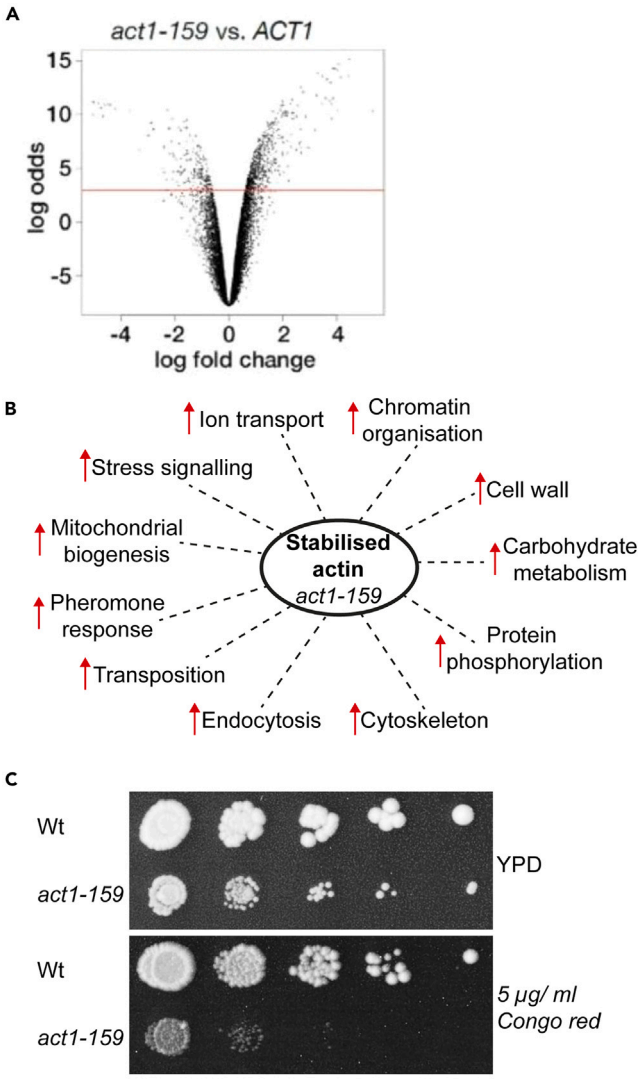

Figure 3. Transcriptional changes in the actin mutant act1-159 suggest involvement of MAPK signaling, flocculation and lipid metabolism

(A and B) Transcriptional changes of act1-159 vs. ACT1 cells grown to log phase in YPD media were investigated by microarray and plotted in a volcano plot. Gene ontology analysis for the GO-term PROCESS was completed using the GO SLIM mapper function available on the *Saccharomyces cerevisiae* genome database[33] and upregulated genes clustered within enriched cellular processes are depicted in panel (B).

(C) Congo red sensitivity of wild type and *act1-159* mutant cells was assessed by a spotting assay using a 10-fold serial dilution series from a starting cell number of 2 x 10^5. See also Table S1.

cof1-5 mutation triggers activation of the CWI MAPK pathway

Our data suggest that cell wall changes observed in *cof1-5* cells are dependent on the presence of VDAC/Por1. As CWI is managed via MAPK signaling, we sought to determine activation of this pathway in *cof1-5* and *cof1-5 por1*Δ cells by immunoblotting for phosphorylation of the terminal MAPK Slt2 at its amino acid residues T190 and Y192.[34] This approach confirmed that Slt2 is constitutively active in *cof1-5* mutant cells and that Slt2 phosphorylation is lost upon deletion of *POR1* in both fermentable (glucose) and non-fermentable (glycerol) carbon source-containing media (Figures 4A and 4B). Constitutive Slt2 phosphorylation in *cof1-5* cells was largely reduced by addition of the Pkc1 inhibitor cercosporamide (CSA), confirming activation of canonical CWI signaling (Figure 4C). Expression of *POR1* from a plasmid led to an increase of Slt2 phosphorylation under all tested conditions and was sufficient to compensate for chromosomal loss of *POR1* (Figure 4D). Unexpectedly, the additional expression of *POR1* from the plasmid on top of basic

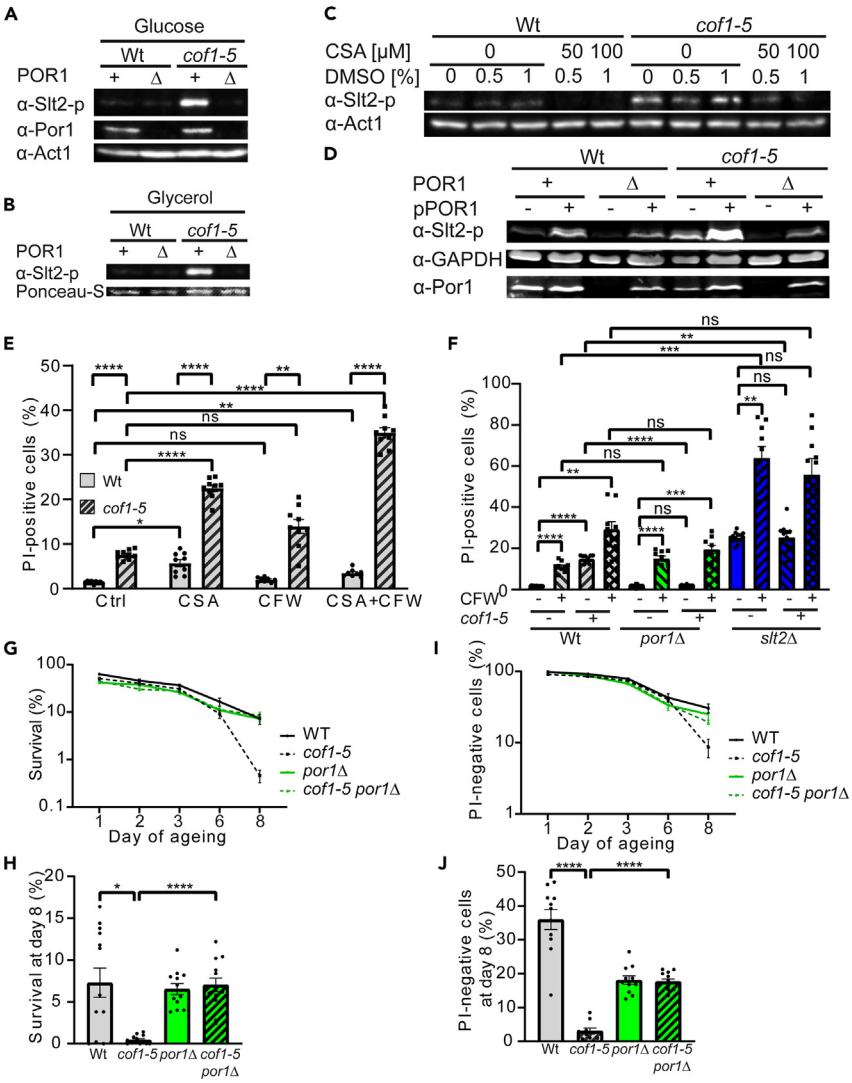

Figure 4. *cof1-5* mutation triggers activation of the CWI pathway

(A and B) Immunoblots detecting Slt2 phosphorylation when grown on glucose and glycerol containing media are shown in A and B, respectively.

(C) Pkc1 inhibition by cercosporamide (CSA) administration prevented Slt2 phosphorylation.

(D) Porin deletion and overexpression reveal dependence of Slt2 phosphorylation on Por1.

(E) *cof1-5* mutation triggers loss of plasma membrane integrity, as assessed flow cytometrically with PI positivity at 48 h after inoculation. PI positivity is exacerbated by additional Pkc1 inhibition using the Pkc1-inhibitor cercosporamide or applying additional cell wall stress with calcofluor white (CFW). Combined treatment with CSA and CFW at the same time shows additive effects.

(F) *POR1* deletion rescues from *cof1-5*-dependent loss of viability and loss of plasma membrane integrity, whereas *SLT2* deletion sensitises to cell death.

(G–J) Chronological aging analysis reveals shortening of chronological lifespan in *cof1-5* cells which depends on *POR1*. Colony forming unit formation based on clonogenic survival is depicted in G and H, whereas PI positivity is shown in I and J. Statistical significance in E, F, H, and J was assessed using Brown-Forsythe and Welch-ANOVA test. Asterisks indicate significance based on p-levels of the comparisons to the respective control strains. See also Figure S2.

Error bars indicate standard error of the mean (SEM) and asterisks indicate significant differences based on p-values, *p < 0.05, **p < 0.01, ***p < 0.001, ****p < 0.0001.

chromosomal expression in wild-type cells was sufficient to trigger CWI signaling (Figure 4D). We further used CFW stress to trigger CWI signaling. We confirmed Slt2 phosphorylation in response to CFW stress in a concentration-dependent manner (Figures S2A–S2C). Basic levels of Slt2 phosphorylation were reduced

in *por1*Δ; however, the strain remained responsive to CFW-induced Slt2 phosphorylation (Figure S2D). Since CWI signaling is a response to stress, we wondered whether its activation in *cof1-5* cells was essential to mediate survival upon cell wall stress. We could confirm that while the *cof1-5* mutation led to an increase in the cell population with loss of plasma membrane integrity, this rose significantly when applying treatment with the Pkc1-inhibitor CSA (Figure 4E). Combined treatment with CSA and CFW, but not CFW alone, led to a further increase in cells exhibiting plasma membrane permeability in an additive manner, suggesting that Pkc1 activity may promote survival when cofilin/actin-induced stress is experienced. We further tested for cell death sensitivity in a genetic model using gene KO strains for *POR1* and *SLT2*. In fact, as expected, *POR1* deletion provided a rescue from *cof1-5*- and CFW-induced cell death, while *SLT2* deletion had the opposite effect (Figure 4F). In wild-type cells CSA treatment or *SLT2* deletion increases the propidium iodide (PI)-positive cell population to 20%, indicating that under basal conditions the CWI pathway is pro-survival. The *cof1-5* mutant shows increased CWI signalling, and the cell population with loss of plasma membrane integrity increases concomitantly. It appears that both a loss and gain of Slt2 phosphorylation could result in increased cell death suggesting a non-linear signaling model for Slt2.

We further conducted chronological aging experiments with PI staining and survival plating as two independent readouts for cell death (Figures 4G and 4H). Importantly, both readouts suggested that *cof1-5*-mediated shortening of the chronological lifespan depends on *POR1*. Welch-ANOVA analysis of survival and PI at day 8 of aging confirmed a significant reduction in survival and PI negativity in *cof1-5* cells, which was rescued by *POR1* deletion (Figures 4I and 4J).

cof1-5 expression prevents Slt2 localization to the nucleus and promotes MAPK signaling from the mitochondrial compartment

Using a wild-type strain expressing Slt2-GFP from its endogenous promoter at its original chromosomal locus, we confirmed that, in line with earlier analyses of Slt2-GFP localization,[35] the majority of cellular Slt2 is found in the nucleus (Figures 5A and 5B). However, in a small proportion (5%) of cells Slt2-GFP could be seen to localize to cytoplasmic foci (Figures 5A and 5C). In contrast, only 1% of *cof1-5* cells showed Slt2 localization to the nucleus (Figure 5B), while a significant proportion (30%) of *cof1-5* cells were observed as having foci (Figures 5A and 5C), and the remaining cells showed diffuse green fluorescence throughout the cytosol.

Given the porin dependence of the CWI activation in *cof1-5* cells, we tested for colocalization with mitochondria using rhodamine B hexylester. Indeed, the Slt2-GFP foci observed in *cof1-5* largely colocalized with rhodamine B hexylester signal after staining (Figures 5D and 5E), whereas no colocalization of Slt2-GFP foci with LDs was detected (Figure S3). We next wanted to assess whether mitochondrial Slt2-GFP foci formation was dependent on Por1. For this purpose, we used an Slt2-GFP expression plasmid. The expression from the plasmid showed a similar result as compared to chromosomal expression, but the percentages of cells with Slt2-GFP foci and nuclear localization in *cof1-5* were roughly doubled (Figures 5F–5H). We reasoned that this was an effect of Slt2-GFP overexpression from the plasmid used. Importantly, additional deletion of *POR1* reduced the fraction of foci-containing cells in *cof1-5* to wild-type levels while at the same time increasing the percentage of cells with nuclear-Slt2-GFP signal to wild-type levels (Figures 5F–5H). The analysis of Slt2-GFP colocalization with mitochondria further supports the latter finding in that the Pearson coefficient is reduced to wild-type levels in *cof1-5 por1*Δ (Figure 5I). Additional analysis of Pkc1-GFP showed a similar pattern of foci formation and colocalization with mitochondria in *cof1-5* as observed when expressing Slt2-GFP (Figures 5J–5L). The percentage of foci-containing cells was increased by roughly 20% in *cof1-5* as compared to wild-type cells (Figure 5K), and the Pearson coefficient of Pkc1 colocalization with mitochondria was significantly increased from 0.26 to 0.59 (Figure 5L).

Altogether this suggests that activation of MAPK signalling in *cof1-5* involves Slt2 and Pkc1 translocation to mitochondria. This further raises the possibility that Slt2-mediated signaling actively occurs at mitochondria.

Reduced actin dynamics lead to a Porin-dependent increase in LD number that is required for CWI activation

Porin has recently been implicated in mitochondrial lipid import.[36] We therefore determined whether LD number and their control were altered in *cof1-5* cells. This idea seemed reasonable since actin and cofilin have been described as regulators of LD homeostasis in mammalian cells.[37–39] We stained cellular LDs of wild-type and *cof1-5* mutants having additional gene-KO deletions encoding for the acyltransferases Lro1 and Dga1 using the specific BODIPY 493/503 dye. LDs of *cof1-5* cells were more abundant than those in

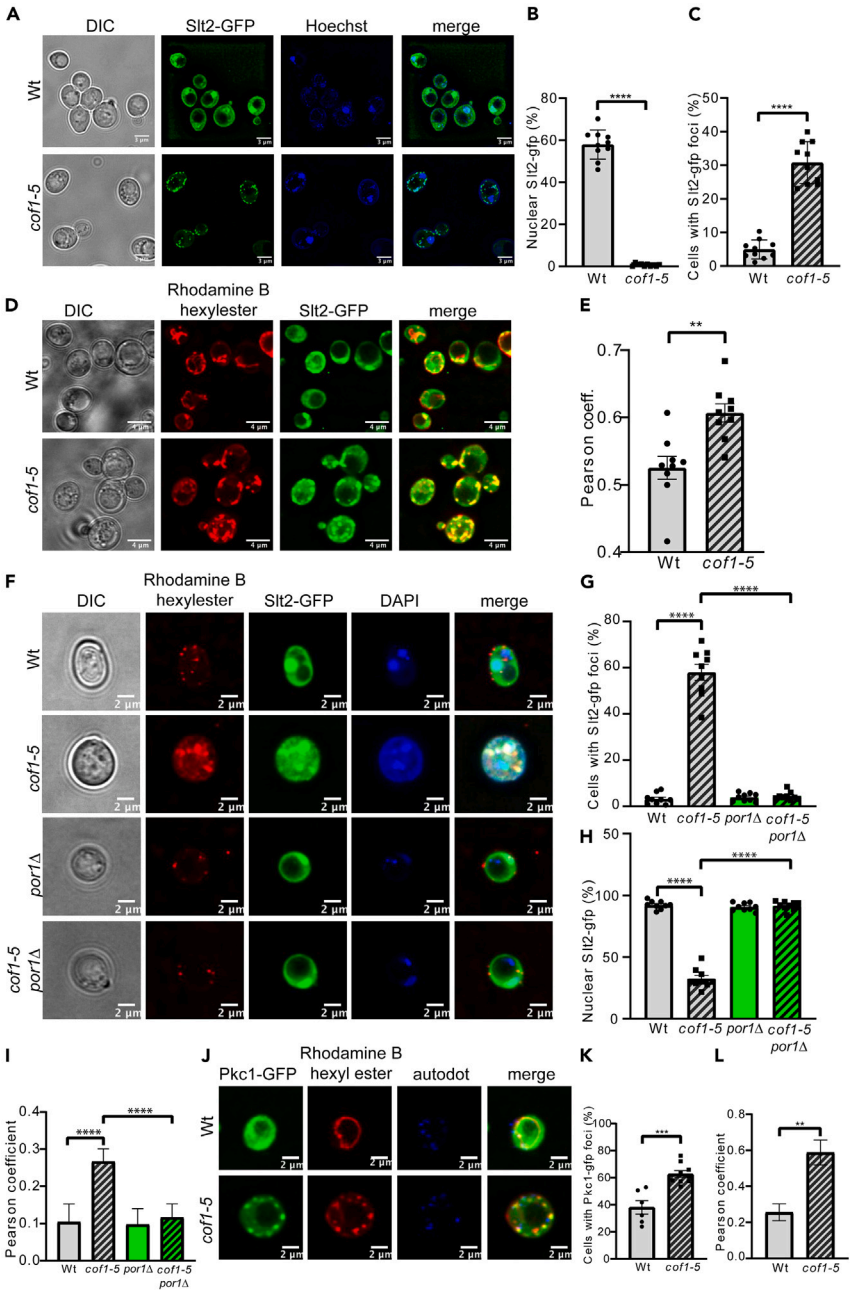

Figure 5. Slt2 localisation to the mitochondrial compartment is enhanced in *cof1-5* cells

(A) Slt2, which is mostly found in the nucleus in wild-type cells at stationary phase, forms punctate foci in *cof1-5*, as documented by fluorescence microscopy using chromosomally tagged SLT2-GFP under control of its endogenous promoter. Deconvolved pictures with Hoechst staining for nuclei are shown.

(B and C) Cells showing nuclear localisation of Slt2-GFP (B) and foci-forming cells (C) were quantified, plotted and analyzed for significant localisation change as compared to wild type.

(D) Representative fluorescence microscopy pictures of Slt2-GFP expressing cells with rhodamine B hexylester staining for colocalization analysis with mitochondria.

(E) Colocalisation of Slt2-GFP (green) with the mitochondrial stain rhodamine B hexylester was increased in *cof1-5* as shown by significant increase of the Pearson colocalisation coefficient.

(F–I) Slt2-GFP expression from a plasmid was used to monitor cellular Slt2 localisation in *cof1-5* cells in dependence of *POR1*. Representative microscopy pictures are shown in (F), Slt-GFP foci-containing cells are quantified in (G), cells with nuclear Slt2 are quantified in (H) and the Pearson coefficient of Slt2-GFP colocalization with mitochondria is visualised in (I).

Figure 5. *Continued*

(J and K) Expression of Pkc1-GFP under control of its endogenous promoter reveals increased PKC1-GFP foci formation in *cof1-5* (J, K). Representative fluorescence microscopy pictures of individual Pkc1-GFP expressing cells with additional rhodamine-B-hexylester staining for mitochondria and autodot staining for LDs are shown in (J) and cells with Pkc1-GFP foci are quantified in (K).

(L) The Pearson coefficient was determined as a measure of colocalisation of Pkc1-GFP with mitochondria (rhodamine-B-hexylester). Statistical significance in (B) and (C) was assessed using Welch's t test, (E, K, L) were analyzed using unpaired t test and (G, H, I) by ordinary one-way ANOVA. See also Figure S3.

Error bars indicate standard error of the mean (SEM) and asterisks indicate significant differences based on p-values, *p < 0.05, **p < 0.01, ***p < 0.001, ****p < 0.0001.

wild-type cells (Figures 6A and 6B). Interestingly, this increase in LD number was reverted when *LRO1* or *DGA1*, or both in combination, was knocked out in *cof1-5* cells (Figures 6A and 6B). Basic levels of Slt2 phosphorylation were significantly decreased in *lro1*Δ and *lro1*Δ *dga1*Δ double knock out (DKO) phenocopying *por1*Δ (Figures S4A and S4B). In addition to that, a non-significant trend in reduced susceptibility to CFW treatment was noted (Figures S4A and S4B). We further found that the increase in LD number in *cof1-5* cells was reversed upon deletion of *POR1* or *SLT2* (Figures 6C, 6D, and S4C). Electron microscopy further supported the hypothesis that LD number is increased in *cof1-5* (Figure 6E) and as a response to CFW treatment (Figure S4D). Some LDs as observed in CFW-treated cells appear to be surrounded by a membrane (Figure S4D). Usually the membranes surrounding LDs identify as ER membranes,[40] which may suggest an increase of LD-ER-membrane contacts.

The acyltransferases Lro1 and Dga1 are required for MAPK-related changes in *cof1-5*

Given these findings, we also investigated whether LD regulation at the stage of fatty acid esterification, via Lro1 and Dga1, would affect CWI signaling or other downstream effects in *cof1-5*. Actin depolarization as observed in *cof1-5* could be rescued neither by *LRO1*- or *DGA1*-single-KOs nor by the DKO, both of which genes encode for acyltransferases (Figure 7A). However, the growth defect (Figure 7B) and the flocculation phenotypes (Figure 7C) of *cof1-5* were compensated by KO of either *LRO1* or *DGA1*. As expected by the rescue of flocculation, the constitutive phosphorylation of Slt2 observed in *cof1-5* cells was turned off upon deletion of *LRO1* or *DGA1* (Figure 7D). We next tested whether diverse stresses such as hydrogen peroxide (H_2O_2), heat, $CuSO_4$, or CFW affected LD abundance. Interestingly, all the stresses triggered an increase in LD abundance with the cell wall stress applied through CFW treatment being strongest (Figure 7E). In summary, this suggests an active role of CWI signaling in the control of lipid metabolism and LD homeostasis downstream or independent of cofilin-mediated actin regulation.

Cofilin and porin are important regulators of lipid homeostasis

With the Porin-dependent changes in LD quantity as observed in *cof1-5* cells, we sought to characterize its effects on global lipid homeostasis. We detected significant changes in *cof1-5* cells for phosphatidylcholine (PC), phosphatidylserine, phosphatidylserine (PS), triglyceride (TG) (Figure 8A), phosphatidic acid (PA), phosphatidylglycerol (PG), lyso-phosphatidylinositol (LPI), ceramide (Figure 8B), sterol esters (SEs) and ergosterol (Erg) (Figure 8C), and the complex sphingolipids mannosyl diphosphoinositol ceramide (MIP2C) and mannosylinositol phosphorylceramide (MIPC) (Figure 8D) when we compared shotgun lipidomic profiles to wild type (additional data on lipid species are available in Figures S5A–S5E). In all cases, with the exception of LPI, all lipid class levels were restored to wild-type levels upon deletion of *POR1*, highlighting the significance of this mitochondrial protein for lipid regulation. The most prominent decrease in *cof1-5* cells was observed for TG. However, additional high-performance thin-layer chromatography (HPTLC) measurements could only confirm a trend in decrease due to strong variation upon the individual samples (Figure 8E). The strongest increases were observed for PA, LPI, SEs, and Erg as well as the complex sphingolipids MIP2C and MIPC. The increases in SE and Erg in *cof1-5* as well as the reduction by the additional gene KOs were confirmed by additional HPTLC quantification and can thus be considered as robust (Figures 8F and 8G). Since the neutral lipids (SE and TG) are stored in LDs, we reasoned that the ratio of SE to TG might correlate with the LD phenotype as observed before. We thus calculated the SE/TG index ($i_{SE/TG}$) and confirmed significant change of the index in *cof1-5* (Figure 8H) which correlates with the increased amount of LDs as quantified in Figures 6A–6D. Interestingly, gene KOs of *POR1, DGA1, LRO1, and* SLT2 revert $i_{SE/TG}$ back to wild-type levels. Further to this, we noted significant lipidomic changes in the *POR1* deletion strain itself (e.g., PC, TG, PA, Cer, CL; Figures 8A and 8B) which confirms that Por1 indeed has crucial impact on total lipid homeostasis.

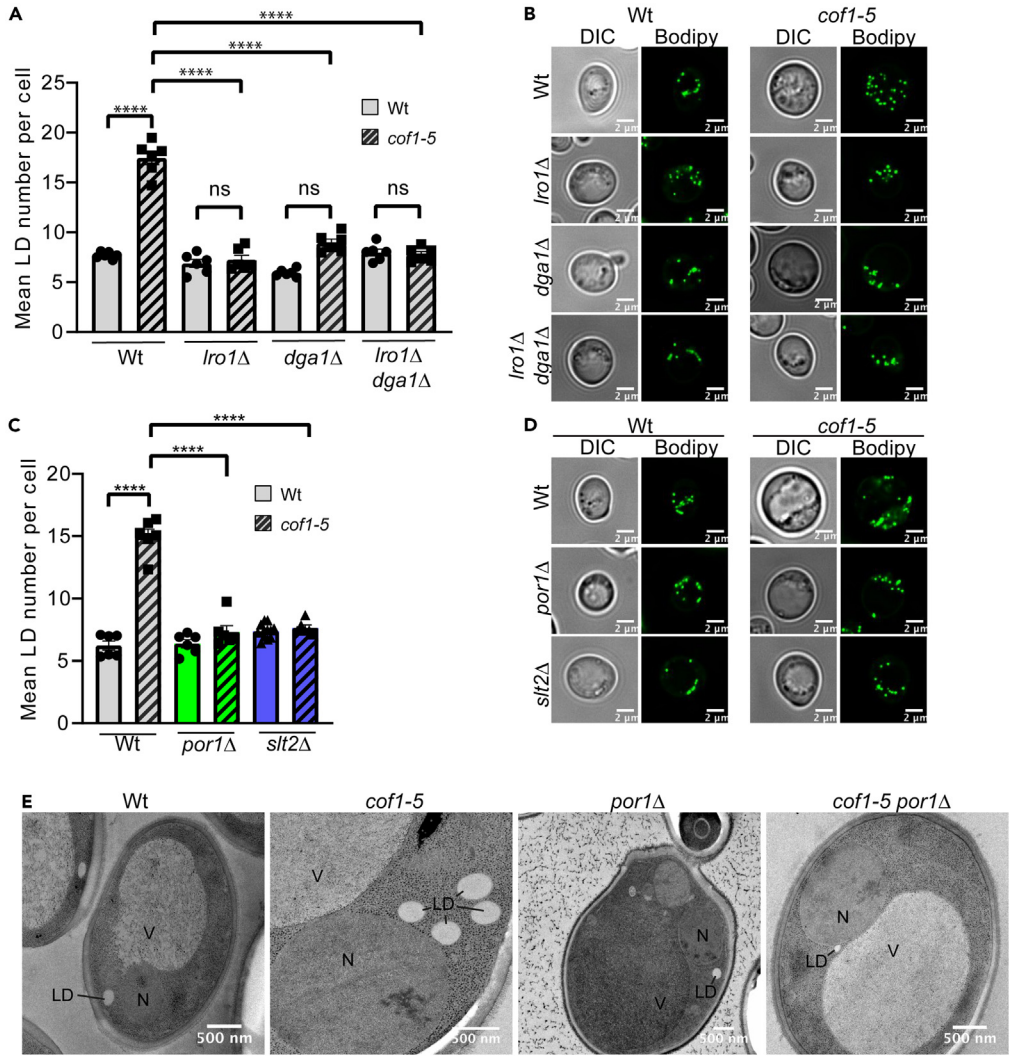

Figure 6. Reduced actin dynamics lead to a porin-dependent increase in lipid droplet number that are required for CWI activation

(A and B) Increase of LD number in *cof1-5* depends on Lro1 and Dga1. Mean LD-numbers per cell are plotted in (A) and representative microscopy pictures are shown in (B). Each dot in (A) represents the mean LD number per cell of a single experiment (n = 6) with at least 119 cells being evaluated per experiment.

(C and D) Gene deletions of *POR1* or *SLT2* are sufficient to prevent LD accumulation in *cof1-5*. Mean LD numbers per cell were assessed by quantifying fluorescence microscopy pictures using Bodipy staining (C). Representative fluorescence microscopy images are shown in (D).

(E) Representative EM micrographs supporting the observation of LD-number-increase in *cof1-5*. V, vacuole; LD, lipid droplet; N, nucleus. Statistical significance in (A) and (C) was assessed using two-way ANOVA with *cof1-5* mutation as first factor and additional KO as second factor. See also Figure S4.

Error bars indicate standard error of the mean (SEM) and asterisks indicate significant differences based on p-values, *p < 0.05, **p < 0.01, ***p < 0.001, ****p < 0.0001.

In summary, these results give evidence that lipidomic changes in *cof1-5* depend on Por1 and further suggest that lipidomic changes in *cof1-5* could be causally linked to CWI signaling.

DISCUSSION

In a healthy dividing yeast cell the experience of a stressor that perturbs the cell wall results in the depolymerization of the F-actin cytoskeleton; this is required to assist in both cell-cycle arrest (G2/M) and the activation of the CWI pathway.[30] We have shown that cells expressing the *cof1-5* mutation, which leads

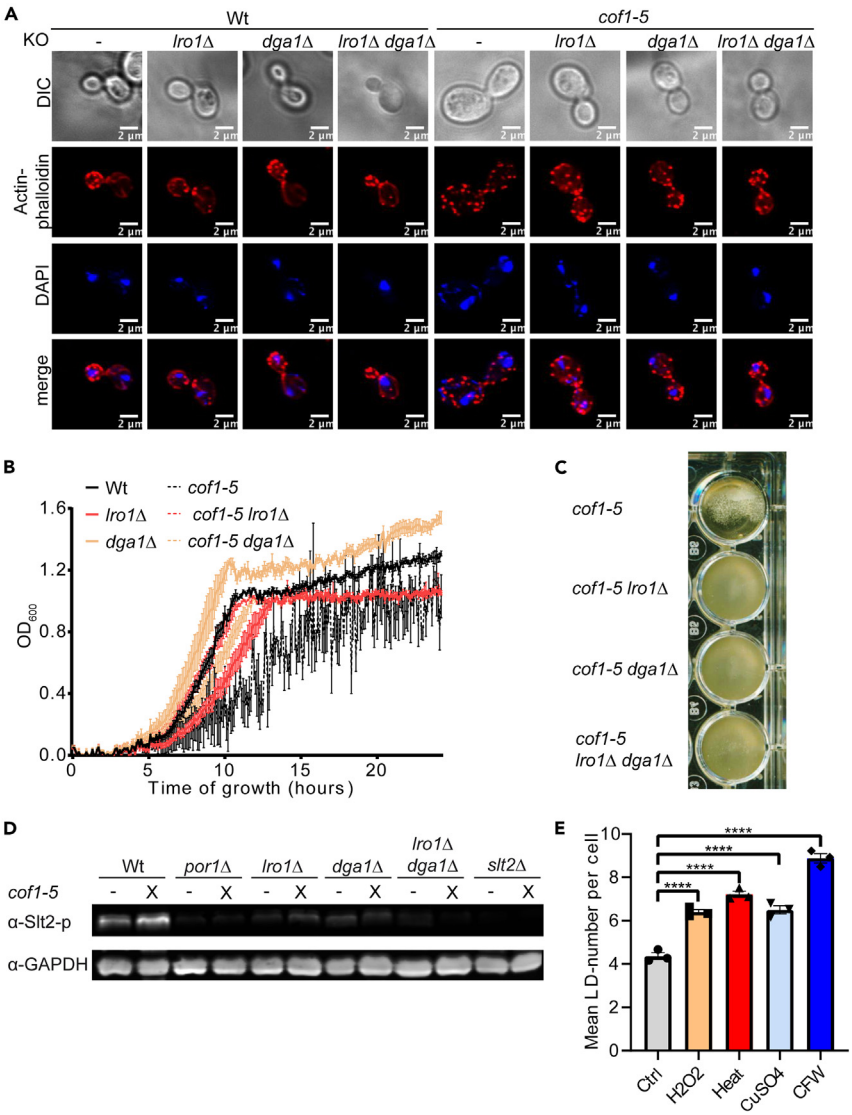

Figure 7. The acyltransferases Lro1 and Dga1 are required for MAPK-related changes in *cof1-5*

(A) Polarisation of the actin cytoskeleton was assessed using phalloidin (red) and DAPI (blue) staining. The *cof1-5* mutant shows loss of actin polarisation, which is not rescued by gene KO of *LRO1*, *DGA1* or a combined double deletion of the ladder.

(B and C) The growth defect (B) and flocculation phenotype (C) as observed in *cof1-5* are restored by additional deletion of the acyltransferases *LRO1*, *DGA1*, or in the double deletion mutant (*lro1*Δ *dga1*Δ).

(D) Slt2 phosphorylation in *cof1-5* depends on Lro1 and Dga1 as the KO of either corresponding gene and the double KO prevents Slt2 phosphorylation.

(E) Mean LD abundance per cell was quantified in diverse conditions of stress. 150 cells per condition and experiment were quantified with a total of three independent experiments (n = 3). Statistical significance in (E) was assessed using ordinary one-way ANOVA.

Error bars indicate standard error of the mean (SEM) and asterisks indicate significant differences based on p-values, *p < 0.05, **p < 0.01, ***p < 0.001, ****p < 0.0001.

to the chronic depolarization of F-actin patches, exhibit hallmarks of constitutive Pkc1/Slt2 activation, such as flocculation and vacuole fragmentation. Our data also show that this aberrant PKC/Slt2 signaling depends on the mitochondrial outer membrane protein Por1, which is the yeast orthologue of mammalian VDAC. Por1 is known to form a pore in the outer mitochondrial membrane thereby facilitating metabolic flux from mitochondria to the cytosol and vice versa.[36,41] Por1 further has been implicated in the control of cell death in response to stress in previous studies.[42,43] However VDAC has also been shown to participate in other cellular processes including the regulation of lipid traffic[36] and in adenosine

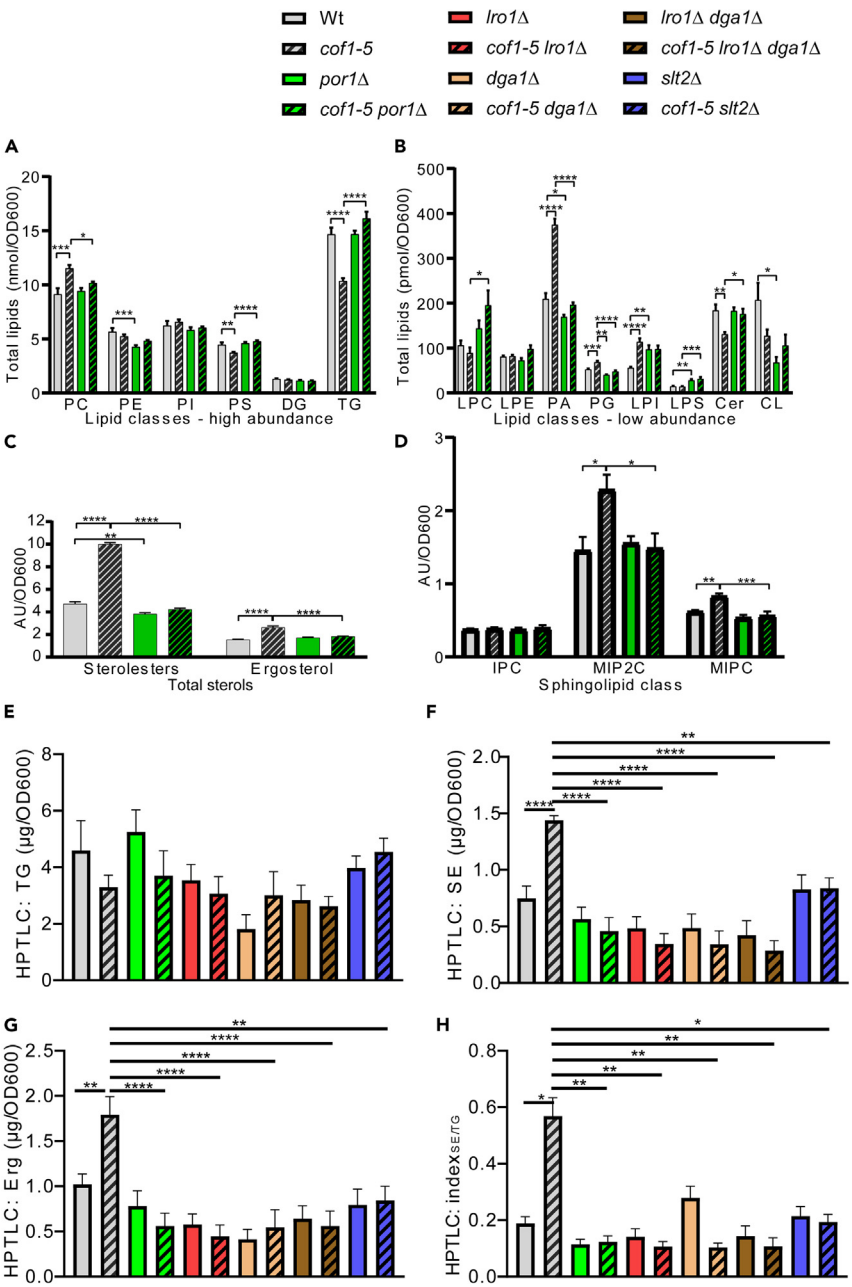

Figure 8. Lipidomic analysis reveals characteristic Por1-dependent changes in the lipid profile of *cof1-5*

(A and B) Mass spectrometry-assisted lipidomic quantification of highly abundant (A) and less abundant yeast lipids from total cell extracts (B).

(C and D) Sterolesters and free ergosterol were quantified separately as shown in (C) and sphingolipids are depicted in (D).

(E–H) Lipidomic changes in the neutral lipid classes TG (E), SE (F), Erg (G) and the index$_{SE/TG}$ (H) were further verified by additional HPTLC analysis. Statistical significance in (A-G) was assessed using two-way ANOVA with *cof1-5* mutation as first factor and additional KO as second factor, except for CL, LPC and LPE in (B), which were analyzed using Kruskal-Wallis test; (H) was analyzed by Brown-Forsythe and Welch ANOVA test. See also Figure S5.

Error bars indicate standard error of the mean (SEM) and asterisks indicate significant differences based on p-values, *p < 0.05, **p < 0.01, ***p < 0.001, ****p < 0.0001.

monophosphate-activated kinase (AMPK/Snf1) signaling.[44–46] Here we show that the actin cytoskeleton and mitochondria coordinate MAPK signaling through VDAC and that this plays a role in cell fate. One possibility is the existence of a physical interaction, as was shown in the case of AMPK/Snf1 signaling,[45]

whereby Slt2 relocates from the nucleus to the mitochondria and docks with VDAC to elicit an alternate signaling response that promotes cell death. In line with this we did observe that the deletion of *POR1* prevented constitutive activation of Slt2 in *cof1-5* cells, restored its localization to the nucleus, and reduced the necrotic cell population. Despite a clear correlation between the prevention of Slt2 activation in *cof1-5* cells by deletion of *POR1*, which led to apparent improvement in cell health, we observed the opposite effect when cells were treated with the PKC inhibitor CSA. This result, while unexpected, may be explained by additional off target effects of CSA, or indeed as a result of functions of PKC that lie outside of the canonical PKC/Slt2 CWI signaling system. Additional evidence to support a direct link from VDAC to Slt2 activation comes from our finding that the overexpression of *POR1* was also sufficient to activate Slt2. Connections between mitochondria and MAPK signaling are emerging; for example, a recent study demonstrated mitochondrial participation in MAPK signaling regulating proteasome granule formation upon carbon starvation.[47]

A number of lipid classes were found to show significant change in the *cof1-5* mutant. These included PC, PS, TG, PA, PG, LPI, ceramide, SEs, Erg, and the complex sphingolipids MIP2C and MIPC (Figures 8A–8D). These changes were largely reversed when *POR1* was knocked out suggesting a clear role for VDAC in the control of lipid homeostasis, possibly via the activation of Slt2. The overall increase in PA might also account for the changes in mitochondrial morphology as this phospholipid has been shown to regulate mitochondrial fusion via control of Ugo1 biogenesis.[48] Mitochondrial phospholipids such as PG and CL have been connected to Pkc1/CWI signaling.[49,50] Loss of CL has also been shown to impair CWI signaling which led to defective mitophagy.[51] We also detected changes in the lipid profile of *POR1*-deleted cells as such, which is in line with recently published findings.[36,52,53] This raises the possibility that actin triggers changes in lipid homeostasis with Porin acting as a central point of lipid flux control, or indeed as a component of the signaling system that regulates lipid homeostasis itself. Interestingly the ERMES, which can facilitate lipid exchange between these compartments, has been implicated in cell death.[54,55]

Our lipidomic results further support the notion that *por1*Δ phenocopies *pgs1*Δ. Pgs1 catalyzes the first step of mitochondrial CL synthesis, which is the phosphorylation of phosphatidylglycerol. *pgs1*Δ has reduced levels of beta-1,3-glucans in its cell wall which is thus defective.[56] Por1 and Por2 have recently been suggested to mediate mitochondrial phospholipid import succumbing to PG and CL synthesis.[36] Our data are in line with these findings and further support the idea of Por1 as a regulator of mitochondrial phospholipid import.

Intriguingly, we found that two acyltransferases Dga1 and Lro1 were also essential for activation of Slt2 and all the downstream phenotypes with the exception of actin depolymerization. Given the changes of LD abundance that we observed upon cell wall stress and found in *cof1-5*-expressing cells, this suggests that CWI signaling involves lipidomic rearrangements and dynamic changes of cellular LDs. Interestingly, the inhibition of actin dynamics through *COF1* depletion has also been shown to disrupt adipogenesis and lipid storage in 3T3-L1 cells.[39]

Our findings that actin and mitochondrial functions are linked to lipid homeostasis in yeast may have relevance for antifungal resistance. Mitochondrial function has been linked to changes in cell wall function and to changes in azole sensitivity, a class of drugs that target Erg synthesis.[57] Erg levels are controlled under normal conditions, but conditions of stress (e.g., osmotic or cell wall stress) can require rapid change in Erg content. A significant increase in Erg esters was observed in *cof1-5* cells (Figures 8C and 8F), suggesting that these cells are dealing with an Erg overflow, thus detoxifying through esterification and storage in LDs. LDs accumulate upon cell wall stress in *cof1-5* cells and in wild-type cells upon CFW stress, where LDs appear to have strong contacts with ER membranes (Figures 6 and S4). One possibility is that actin and cofilin are needed to facilitate non-vesicular sterol transport by Osh and Lam proteins.[58–60] Another possibility is that, through activation of the CWI pathway, Pkc1 can phosphorylate Pah1[61,62] (which dephosphorylates PA to yield diacylglycerol) leading to its degradation by the proteasome.[63] This in turn would increase PA levels and decrease TG at the same time which is what we observe in *cof1-5*-expressing cells. Of note, deletion of *pah1* has been described to shorten chronological lifespan,[64] which suggests a pro-death trigger upon loss of Pah1 function. Since Pah1 activity has been described to be essential for homotypic vacuole fusion,[65] this also offers an explanation for the fragmented vacuole phenotype as we observed in *cof1-5* cells. Indeed, the fragmented vacuoles of *cof1-5* look very similar to vacuoles as observed in *pah1*Δ or propranolol-treated cells, which represents a pharmacological treatment to inhibit

Pah1 activity.[65] The increase in Erg as well as the increase in complex sphingolipids observed in *cof1-5*-expressing cells may represent an adaptation to overcome mechanical stress at the plasma membrane. Generally the integration of complex sphingolipids together with sterols results in increased packaging and thus higher density which renders the plasma membrane more resistant to mechanical stress.[66] Thus, the activation of Slt2 in actin-stabilized cells may contribute to the cell's response to stress and so survival in the short term. However, as such cells are clearly sensitive to additional stress, we favor an interpretation that chronic actin depolymerization in dividing cells promotes necrotic cell death.

Permeabilization of the vacuole is a feature of regulated cell death in yeast, which through vacuolar release of Pep4, an orthologue of human cathepsin D, into the cytosol succumbs to cell death.[67–69] More recently a molecular pathway of how vacuole membrane permeabilization is established in yeast was proposed.[70] The vacuolar phenotype as observed in *cof1-5* cells in our study might have similarity to the previously described cell death routines but additionally involves mitochondrial Por1 activity and lipid metabolism. Further investigation will be required to test this possibility.

In summary, our study provides further evidence that the regulation of actin dynamics is crucial for cell fate determination. We show that a reduced ability to regulate actin in dividing yeast cells leads to a pro-death mode of MAPK signaling under conditions of stress. We would argue that this represents a mechanism by which cells that are unable to regulate actin may be lost within a population of cells, such as a colony or biofilm, and postulate that this may represent a novel cell death mechanism in yeast that helps ensure clonal integrity.

Limitations of the study

The authors recognize that this study opens a number of questions that arise as a consequence of unrecognized interplay between lipid homeostasis, membrane organization, and cell signaling systems in yeast. Further investigations that we suggest within the discussion section highlight a current need to improve our understanding of lipid regulation within eukaryotic cells. A further limitation lies within our current understanding of yeast cell death as a regulated process. Although there is strong evidence to suggest that different modes of death exist, the experimental tools available to differentiate between programmed and passive cell death in yeast are, in the authors' view, limited at the time of writing. This led to a conservative interpretation of the data presented as a loss of cellular integrity as opposed to a mechanism of regulated cell death.

STAR★METHODS

Detailed methods are provided in the online version of this paper and include the following:

- KEY RESOURCES TABLE
- RESOURCE AVAILABILITY
  - Lead contact
  - Materials availability
  - Data and code availability
- EXPERIMENTAL MODEL AND SUBJECT DETAILS
- METHOD DETAILS
  - Growth assays
  - Analysis of cell viability, density and diameter
  - Fluorescence microscopy
  - RNA isolation and microarray
  - Immunoblotting
  - Lipid extraction and quantification by shotgun mass spectrometry
  - Lipid extraction and quantification by thin-layer chromatography
  - Electron microscopy high pressure freezing with a Leica EM HPM 100 and freeze substitution
- QUANTIFICATION AND STATISTICAL ANALYSIS

SUPPLEMENTAL INFORMATION

Supplemental information can be found online at https://doi.org/10.1016/j.isci.2023.107539.

ACKNOWLEDGMENTS

We thank Pekka Lappalainen and David Drubin for providing the *cof1-5* and *act1-159* mutant strains. The pRS426-SLT2-GFP plasmid was a kind gift from Matthias Peter and pYX122-mtGFP from Benedikt Westermann. We are thankful to Dominique Pernitsch and Kerstin Hingerl for technical assistance in electron microscopy. P.R. and C.W.G. were supported by the Erwin Schrödinger Fellowship from the Austrian Science Fund (FWF) (J3742-B28) and the University of Kent. P.R. is supported by the "NRW Rückkehr Programm" from the Ministry of Culture and Science of the German State of North Rhine-Westphalia".

AUTHOR CONTRIBUTIONS

Conceptualization, C.W.G. and P.R.; Methodology, J.D., T.M., M.S., D.S., L.N., J.H., F.B., E.S.M.E., O.K., D.G., T.vd.H, C.W.G., and P.R.; Validation, J.D., T.M., M.S., O.K., C.W.G., and P.R.; Formal Analysis, J.D., T.M., M.S., O.K., and P.R.; Investigation, J.D., T.M., M.S., D.S., L.N., J.H., F.B., E.S.M.E., O.K., and P.R.; Data Curation, P.R.; Writing-Original Draft Preparation, C.W.G. and P.R.; Writing-Review and Editing, J.D., T.M., M.S., and O.K.; Figure Visualization, C.W.G. and P.R.; Supervision, Project Administration, and Funding Acquisition, C.W.G. and P.R. All authors have read and agreed to the published version of the manuscript.

DECLARATION OF INTERESTS

The authors declare no competing interests.

INCLUSION AND DIVERSITY

We support inclusive, diverse, and equitable conduct of research.

Received: March 23, 2023
Revised: July 14, 2023
Accepted: July 28, 2023
Published: August 2, 2023

REFERENCES

1. Mishra, M., Huang, J., and Balasubramanian, M.K. (2014). The yeast actin cytoskeleton. FEMS Microbiol. Rev. *38*, 213–227. https://doi.org/10.1111/1574-6976.12064.

2. Ren, W., Zhao, W., Cao, L., and Huang, J. (2020). Involvement of the Actin Machinery in Programmed Cell Death. Front. Cell Dev. Biol. *8*, 634849. https://doi.org/10.3389/fcell.2020.634849.

3. Bamburg, J.R., and Bernstein, B.W. (2008). ADF/Cofilin. Curr. Biol. *18*, R273–R275. https://doi.org/10.1016/j.cub.2008.02.002.

4. Klamt, F., Zdanov, S., Levine, R.L., Pariser, A., Zhang, Y., Zhang, B., Yu, L.-R., Veenstra, T.D., and Shacter, E. (2009). Oxidant-induced apoptosis is mediated by oxidation of the actin-regulatory protein cofilin. Nat. Cell Biol. *11*, 1241–1246. https://doi.org/10.1038/ncb1968.

5. Bamburg, J.R., and Wiggan, O.P. (2002). ADF/cofilin and actin dynamics in disease. Trends Cell Biol. *12*, 598–605. https://doi.org/10.1016/S0962-8924(02)02404-2.

6. Kotiadis, V.N., Leadsham, J.E., Bastow, E.L., Gheeraert, A., Whybrew, J.M., Bard, M., Lappalainen, P., and Gourlay, C.W. (2012). Identification of new surfaces of cofilin that link mitochondrial function to the control of multi-drug resistance. J. Cell Sci. *125*, 2288–2299. https://doi.org/10.1242/jcs.099390.

7. Galluzzi, L., Vitale, I., Aaronson, S.A., Abrams, J.M., Adam, D., Agostinis, P., Alnemri, E.S., Altucci, L., Amelio, I., Andrews, D.W., et al. (2018). Molecular mechanisms of cell death: recommendations of the Nomenclature Committee on Cell Death 2018. Cell Death Differ. *25*, 486–541. https://doi.org/10.1038/s41418-017-0012-4.

8. Madeo, F., Fröhlich, E., and Fröhlich, K.U. (1997). A Yeast Mutant Showing Diagnostic Markers of Early and Late Apoptosis. J. Cell Biol. *139*, 729–734.

9. Büttner, S., Eisenberg, T., Herker, E., Carmona-Gutierrez, D., Kroemer, G., and Madeo, F. (2006). Why yeast cells can undergo apoptosis: death in times of peace, love, and war. J. Cell Biol. *175*, 521–525. https://doi.org/10.1083/jcb.200608098.

10. Carmona-Gutierrez, D., Bauer, M.A., Zimmermann, A., Aguilera, A., Austriaco, N., Ayscough, K., Balzan, R., Bar-Nun, S., Barrientos, A., Belenky, P., et al. (2018). Guidelines and recommendations on yeast cell death nomenclature. Microb. Cell *5*, 4–31. https://doi.org/10.15698/mic2018.01.607.

11. Rockenfeller, P., Ring, J., Muschett, V., Beranek, A., Büttner, S., Carmona-Gutierrez, D., Eisenberg, T., Khoury, C., Rechberger, G., Kohlwein, S.D., et al. (2010). Fatty acids trigger mitochondrion-dependent necrosis. Cell Cycle *9*, 2908–2914. https://doi.org/10.4161/cc.9.14.12346.

12. Rockenfeller, P., Smolnig, M., Diessl, J., Bashir, M., Schmiedhofer, V., Knittelfelder, O., Ring, J., Franz, J., Foessl, I., Khan, M.J., et al. (2018). Diacylglycerol triggers Rim101 pathway–dependent necrosis in yeast: a model for lipotoxicity. Cell Death Differ. *25*, 767–783. https://doi.org/10.1038/s41418-017-0014-2.

13. Rockenfeller, P., and Gourlay, C.W. (2018). Lipotoxicty in yeast: a focus on plasma membrane signalling and membrane contact sites. FEMS Yeast Res. *18*, foy034. https://doi.org/10.1093/femsyr/foy034.

14. Carmona-Gutierrez, D., Reisenbichler, A., Heimbucher, P., Bauer, M.A., Braun, R.J., Ruckenstuhl, C., Büttner, S., Eisenberg, T., Rockenfeller, P., Fröhlich, K.U., et al. (2011). Ceramide triggers metacaspase-independent mitochondrial cell death in yeast. Cell Cycle *10*, 3973–3978. https://doi.org/10.4161/cc.10.22.18212.

15. Lappalainen, P., Fedorov, E.V., Fedorov, A.A., Almo, S.C., and Drubin, D.G. (1997). Essential functions and actin-binding surfaces of yeast cofilin revealed by systematic mutagenesis. EMBO J. *16*, 5520–5530. https://doi.org/10.1093/emboj/16.18.5520.

16. González-Rubio, G., Sastre-Vergara, L., Molina, M., Martín, H., and Fernández-Acero, T. (2022). Substrates of the MAPK Slt2: Shaping Yeast Cell Integrity. J. Fungi *8*, 368. https://doi.org/10.3390/jof8040368.

17. Takasaki, T., Utsumi, R., Shimada, E., Bamba, A., Hagihara, K., Satoh, R., and Sugiura, R. (2023). Atg1, a key regulator of autophagy, functions to promote MAPK activation and cell death upon calcium overload in fission yeast. Microb. Cell *10*, 133–140. https://doi.org/10.15698/mic2023.06.798.

18. Rego, A., Duarte, A.M., Azevedo, F., Sousa, M.J., Côrte-Real, M., and Chaves, S.R. (2014). Cell wall dynamics modulate acetic acid-induced apoptotic cell death of Saccharomyces cerevisiae. Microb. Cell *1*, 303–314. https://doi.org/10.15698/mic2014.09.164.

19. Kanda, Y., Satoh, R., Takasaki, T., Tomimoto, N., Tsuchiya, K., Tsai, C.A., Tanaka, T., Kyomoto, S., Hamada, K., Fujiwara, T., and Sugiura, R. (2021). Sequestration of the PKC ortholog Pck2 in stress granules as a feedback mechanism of MAPK signaling in fission yeast. J. Cell Sci. *134*, jcs250191. https://doi.org/10.1242/jcs.250191.

20. Illescas, M., Peñas, A., Arenas, J., Martín, M.A., and Ugalde, C. (2021). Regulation of Mitochondrial Function by the Actin Cytoskeleton. Front. Cell Dev. Biol. *9*, 795838. https://doi.org/10.3389/fcell.2021.795838.

21. Adams, A.E., and Pringle, J.R. (1984). Relationship of actin and tubulin distribution to bud growth in wild- type and morphogenetic-mutant Saccharomyces cerevisiae. J. Cell Biol. *98*, 934–945.

22. Kilmartin, J.V., and Adams, A.E. (1984). Structural rearrangements of tubulin and actin during the cell cycle of the yeast Saccharomyces. J. Cell Biol. *98*, 922–933.

23. Mulholland, J., Preuss, D., Moon, A., Wong, A., Drubin, D., and Botstein, D. (1994). Ultrastructure of the yeast actin cytoskeleton and its association with the plasma membrane. J. Cell Biol. *125*, 381–391.

24. Novick, P., and Botstein, D. (1985). Phenotypic analysis of temperature-sensitive yeast actin mutants. Cell *40*, 405–416. https://doi.org/10.1016/0092-8674(85)90154-0.

25. Lappalainen, P., and Drubin, D.G. (1997). Cofilin promotes rapid actin filament turnover *in vivo*. Nature *388*, 78–82. https://doi.org/10.1038/40418.

26. Kornmann, B., Currie, E., Collins, S.R., Schuldiner, M., Nunnari, J., Weissman, J.S., and Walter, P. (2009). An ER-Mitochondria Tethering Complex Revealed by a Synthetic Biology Screen. Science *325*, 477–481. https://doi.org/10.1126/science.1175088.

27. Soares, E.V. (2011). Flocculation in Saccharomyces cerevisiae: a review. J. Appl. Microbiol. *110*, 1–18. https://doi.org/10.1111/j.1365-2672.2010.04897.x.

28. Sariki, S.K., Kumawat, R., Singh, V., and Tomar, R.S. (2019). Flocculation of Saccharomyces cerevisiae is dependent on activation of Slt2 and Rlm1 regulated by the cell wall integrity pathway. Mol. Microbiol. *112*, 1350–1369. https://doi.org/10.1111/mmi.14375.

29. Free, S.J. (2013). Chapter Two - Fungal Cell Wall Organization and Biosynthesis. In Advances in Genetics, T. Friedmann, J.C. Dunlap, and S.F. Goodwin, eds. (Academic Press), pp. 33–82. https://doi.org/10.1016/B978-0-12-407677-8.00002-6.

30. Levin, D.E. (2011). Regulation of Cell Wall Biogenesis in Saccharomyces cerevisiae: The Cell Wall Integrity Signaling Pathway. Genetics *189*, 1145–1175. https://doi.org/10.1534/genetics.111.128264.

31. Elorza, M.V., Rico, H., and Sentandreu, R. (1983). Calcofluor white alters the assembly of chitin fibrils in Saccharomyces cerevisiae and Candida albicans cells. J. Gen. Microbiol. *129*, 1577–1582. https://doi.org/10.1099/00221287-129-5-1577.

32. Belmont, L.D., and Drubin, D.G. (1998). The Yeast V159N Actin Mutant Reveals Roles for Actin Dynamics In Vivo. J. Cell Biol. *142*, 1289–1299.

33. Cherry, J.M., Hong, E.L., Amundsen, C., Balakrishnan, R., Binkley, G., Chan, E.T., Christie, K.R., Costanzo, M.C., Dwight, S.S., Engel, S.R., et al. (2012). Saccharomyces Genome Database: the genomics resource of budding yeast. Nucleic Acids Res. *40*, D700–D705. https://doi.org/10.1093/nar/gkr1029.

34. Lee, K.S., Irie, K., Gotoh, Y., Watanabe, Y., Araki, H., Nishida, E., Matsumoto, K., and Levin, D.E. (1993). A yeast mitogen-activated protein kinase homolog (Mpk1p) mediates signalling by protein kinase C. Mol. Cell Biol. *13*, 3067–3075.

35. van Drogen, F., and Peter, M. (2002). Spa2p Functions as a Scaffold-like Protein to Recruit the Mpk1p MAP Kinase Module to Sites of Polarized Growth. Curr. Biol. *12*, 1698–1703. https://doi.org/10.1016/S0960-9822(02)01186-7.

36. Miyata, N., Fujii, S., and Kuge, O. (2018). Porin proteins have critical functions in mitochondrial phospholipid metabolism in yeast. J. Biol. Chem. *293*, 17593–17605. https://doi.org/10.1074/jbc.RA118.005410.

37. Pfisterer, S.G., Gateva, G., Horvath, P., Pirhonen, J., Salo, V.T., Karhinen, L., Varjosalo, M., Ryhänen, S.J., Lappalainen, P., and Ikonen, E. (2017). Role for formin-like 1-dependent acto-myosin assembly in lipid droplet dynamics and lipid storage. Nat. Commun. *8*, 14858. https://doi.org/10.1038/ncomms14858.

38. Weibel, G.L., Joshi, M.R., Jerome, W.G., Bates, S.R., Yu, K.J., Phillips, M.C., and Rothblat, G.H. (2012). Cytoskeleton Disruption in J774 Macrophages: Consequences for Lipid Droplet Formation and Cholesterol Flux. Biochim. Biophys. Acta *1821*, 464–472. https://doi.org/10.1016/j.bbalip.2011.09.015.

39. Yang, W., Thein, S., Wang, X., Bi, X., Ericksen, R.E., Xu, F., and Han, W. (2014). BSCL2/seipin regulates adipogenesis through actin cytoskeleton remodelling. Hum. Mol. Genet. *23*, 502–513. https://doi.org/10.1093/hmg/ddt444.

40. Choudhary, V., and Schneiter, R. (2020). Lipid droplet biogenesis from specialized ER subdomains. Microb. Cell *7*, 218–221. https://doi.org/10.15698/mic2020.08.727.

41. Lee, A.C., Xu, X., Blachly-Dyson, E., Forte, M., and Colombini, M. (1998). The role of yeast VDAC genes on the permeability of the mitochondrial outer membrane. J. Membr. Biol. *161*, 173–181.

42. Trindade, D., Pereira, C., Chaves, S.R., Manon, S., Côrte-Real, M., and Sousa, M.J. (2016). VDAC regulates AAC-mediated apoptosis and cytochrome c release in yeast. Microb. Cell *3*, 500–510. https://doi.org/10.15698/mic2016.10.533.

43. Tulha, J., and Lucas, C. (2018). Saccharomyces cerevisiae mitochondrial Por1/yVDAC1 (voltage-dependent anion channel 1) interacts physically with the MBOAT O-acyltransferase Gup1/HHATL in the control of cell wall integrity and programmed cell death. FEMS Yeast Res. *18*, foy097. https://doi.org/10.1093/femsyr/foy097.

44. Bobba, A., Casalino, E., Amadoro, G., Petragallo, V.A., and Atlante, A. (2017). AMPK is activated early in cerebellar granule cells undergoing apoptosis and influences VADC1 phosphorylation status and activity. Apoptosis *22*, 1069–1078. https://doi.org/10.1007/s10495-017-1389-8.

45. Strogolova, V., Orlova, M., Shevade, A., and Kuchin, S. (2012). Mitochondrial Porin Por1 and Its Homolog Por2 Contribute to the Positive Control of Snf1 Protein Kinase in Saccharomyces cerevisiae. Eukaryot. Cell *11*, 1568–1572. https://doi.org/10.1128/EC.00127-12.

46. Shevade, A., Strogolova, V., Orlova, M., Yeo, C.T., and Kuchin, S. (2018). Mitochondrial Voltage-Dependent Anion Channel Protein Por1 Positively Regulates the Nuclear Localization of Saccharomyces cerevisiae AMP-Activated Protein Kinase. mSphere *3*, e00482-17. https://doi.org/10.1128/mSphere.00482-17.

47. Waite, K.A., and Roelofs, J. (2022). Proteasome granule formation is regulated through mitochondrial respiration and kinase signaling. J. Cell Sci. *135*, jcs259778. https://doi.org/10.1242/jcs.259778.

48. Vögtle, F.N., Keller, M., Taskin, A.A., Horvath, S.E., Guan, X.L., Prinz, C., Opalińska, M., Zorzin, C., van der Laan, M., Wenk, M.R., et al. (2015). The fusogenic lipid phosphatidic acid promotes the biogenesis of mitochondrial outer membrane protein Ugo1. J. Cell Biol. *210*, 951–960. https://doi.org/10.1083/jcb.201506085.

49. Zhong, Q., Li, G., Gvozdenovic-Jeremic, J., and Greenberg, M.L. (2007). Up-regulation of the Cell Integrity Pathway in Saccharomyces cerevisiae Suppresses

Temperature Sensitivity of the pgs1Δ Mutant. J. Biol. Chem. *282*, 15946–15953. https://doi.org/10.1074/jbc.M701055200.

50. Nunez, L.R., Jesch, S.A., Gaspar, M.L., Almaguer, C., Villa-Garcia, M., Ruiz-Noriega, M., Patton-Vogt, J., and Henry, S.A. (2008). Cell Wall Integrity MAPK Pathway Is Essential for Lipid Homeostasis. J. Biol. Chem. *283*, 34204–34217. https://doi.org/10.1074/jbc.M806391200.

51. Shen, Z., Li, Y., Gasparski, A.N., Abeliovich, H., and Greenberg, M.L. (2017). Cardiolipin regulates mitophagy through the PKC pathway. J. Biol. Chem. *292*, 2916–2923. https://doi.org/10.1074/jbc.M116.753574.

52. Broeskamp, F., Edrich, E.S.M., Knittelfelder, O., Neuhaus, L., Meyer, T., Heyden, J., Habernig, L., Kreppel, F., Gourlay, C.W., and Rockenfeller, P. (2021). Porin 1 Modulates Autophagy in Yeast. Cells *10*, 2416. https://doi.org/10.3390/cells10092416.

53. Ellenrieder, L., Dieterle, M.P., Doan, K.N., Mårtensson, C.U., Floerchinger, A., Campo, M.L., Pfanner, N., and Becker, T. (2019). Dual Role of Mitochondrial Porin in Metabolite Transport across the Outer Membrane and Protein Transfer to the Inner Membrane. Mol. Cell *73*, 1056–1065.e7. https://doi.org/10.1016/j.molcel.2018.12.014.

54. Martins, V.M., Fernandes, T.R., Lopes, D., Afonso, C.B., Domingues, M.R.M., Côrte-Real, M., and Sousa, M.J. (2019). Contacts in Death: The Role of the ER–Mitochondria Axis in Acetic Acid-Induced Apoptosis in Yeast. J. Mol. Biol. *431*, 273–288. https://doi.org/10.1016/j.jmb.2018.11.002.

55. Smethurst, D.G.J., and Cooper, K.F. (2017). ER fatalities-The role of ER-mitochondrial contact sites in yeast life and death decisions. Mech. Ageing Dev. *161*, 225–233. https://doi.org/10.1016/j.mad.2016.07.007.

56. Zhong, Q., Gvozdenovic-Jeremic, J., Webster, P., Zhou, J., and Greenberg, M.L. (2005). Loss of Function of KRE5 Suppresses Temperature Sensitivity of Mutants Lacking Mitochondrial Anionic Lipids. Mol. Biol. Cell *16*, 665–675. https://doi.org/10.1091/mbc.E04-09-0808.

57. Dagley, M.J., Gentle, I.E., Beilharz, T.H., Pettolino, F.A., Djordjevic, J.T., Lo, T.L., Uwamahoro, N., Rupasinghe, T., Tull, D.L., McConville, M., et al. (2011). Cell wall integrity is linked to mitochondria and phospholipid homeostasis in Candida albicans through the activity of the post-transcriptional regulator Ccr4-Pop2. Mol. Microbiol. *79*, 968–989. https://doi.org/10.1111/j.1365-2958.2010.07503.x.

58. Gatta, A.T., Wong, L.H., Sere, Y.Y., Calderón-Noreña, D.M., Cockcroft, S., Menon, A.K., and Levine, T.P. (2015). A new family of StART domain proteins at membrane contact sites has a role in ER-PM sterol transport. Elife *4*, e07253. https://doi.org/10.7554/eLife.07253.

59. Quon, E., Nenadic, A., Zaman, M.F., Johansen, J., and Beh, C.T. (2022). ER-PM membrane contact site regulation by yeast ORPs and membrane stress pathways. PLoS Genet. *18*, e1010106. https://doi.org/10.1371/journal.pgen.1010106.

60. Sokolov, S.S., Trushina, N.I., Severin, F.F., and Knorre, D.A. (2019). Ergosterol Turnover in Yeast: An Interplay between Biosynthesis and Transport. Biochemistry *84*, 346–357. https://doi.org/10.1134/S0006297919040023.

61. Dey, P., Su, W.-M., Han, G.-S., and Carman, G.M. (2017). Phosphorylation of lipid metabolic enzymes by yeast protein kinase C requires phosphatidylserine and diacylglycerol. J. Lipid Res. *58*, 742–751. https://doi.org/10.1194/jlr.M075036.

62. Su, W.-M., Han, G.-S., and Carman, G.M. (2014). Cross-talk Phosphorylations by Protein Kinase C and Pho85p-Pho80p Protein Kinase Regulate Pah1p Phosphatidate Phosphatase Abundance in Saccharomyces cerevisiae. J. Biol. Chem. *289*, 18818–18830. https://doi.org/10.1074/jbc.M114.581462.

63. Hsieh, L.-S., Su, W.-M., Han, G.-S., and Carman, G.M. (2015). Phosphorylation Regulates the Ubiquitin-independent Degradation of Yeast Pah1 Phosphatidate Phosphatase by the 20S Proteasome. J. Biol. Chem. *290*, 11467–11478. https://doi.org/10.1074/jbc.M115.648659.

64. Park, Y., Han, G.-S., Mileykovskaya, E., Garrett, T.A., and Carman, G.M. (2015). Altered Lipid Synthesis by Lack of Yeast Pah1 Phosphatidate Phosphatase Reduces Chronological Life Span. J. Biol. Chem. *290*, 25382–25394. https://doi.org/10.1074/jbc.M115.680314.

65. Sasser, T., Qiu, Q.-S., Karunakaran, S., Padolina, M., Reyes, A., Flood, B., Smith, S., Gonzales, C., and Fratti, R.A. (2012). Yeast Lipin 1 Orthologue Pah1p Regulates Vacuole Homeostasis and Membrane Fusion. J. Biol. Chem. *287*, 2221–2236. https://doi.org/10.1074/jbc.M111.317420.

66. van Meer, G., Voelker, D.R., and Feigenson, G.W. (2008). Membrane lipids: where they are and how they behave. Nat. Rev. Mol. Cell Biol. *9*, 112–124. https://doi.org/10.1038/nrm2330.

67. Mason, D.A., Shulga, N., Undavai, S., Ferrando-May, E., Rexach, M.F., and Goldfarb, D.S. (2005). Increased nuclear envelope permeability and Pep4p-dependent degradation of nucleoporins during hydrogen peroxide-induced cell death. FEMS Yeast Res. *5*, 1237–1251. https://doi.org/10.1016/j.femsyr.2005.07.008.

68. Sousa, M.J., Azevedo, F., Pedras, A., Marques, C., Coutinho, O.P., Preto, A., Gerós, H., Chaves, S.R., and Côrte-Real, M. (2011). Vacuole-mitochondrial cross-talk during apoptosis in yeast: a model for understanding lysosome-mitochondria-mediated apoptosis in mammals. Biochem. Soc. Trans. *39*, 1533–1537. https://doi.org/10.1042/BST0391533.

69. Pereira, C., Chaves, S., Alves, S., Salin, B., Camougrand, N., Manon, S., Sousa, M.J., and Côrte-Real, M. (2010). Mitochondrial degradation in acetic acid-induced yeast apoptosis: the role of Pep4 and the ADP/ATP carrier. Mol. Microbiol. *76*, 1398–1410. https://doi.org/10.1111/j.1365-2958.2010.07122.x.

70. Stolp, Z.D., Kulkarni, M., Liu, Y., Zhu, C., Jalisi, A., Lin, S., Casadevall, A., Cunningham, K.W., Pineda, F.J., Teng, X., and Hardwick, J.M. (2022). Yeast cell death pathway requiring AP-3 vesicle trafficking leads to vacuole/lysosome membrane permeabilization. Cell Rep. *39*, 110647. https://doi.org/10.1016/j.celrep.2022.110647.

71. Westermann, B., and Neupert, W. (2000). Mitochondria-targeted green fluorescent proteins: convenient tools for the study of organelle biogenesis in Saccharomyces cerevisiae. Yeast *16*, 1421–1427. https://doi.org/10.1002/1097-0061(200011)16:15<1421::AID-YEA624>3.0.CO;2-U.

72. Bähler, J., Wu, J.-Q., Longtine, M.S., Shah, N.G., Iii, A.M., Steever, A.B., Wach, A., Philippsen, P., and Pringle, J.R. (1998). Heterologous modules for efficient and versatile PCR-based gene targeting in Schizosaccharomyces pombe. Yeast *14*, 943–951. https://doi.org/10.1002/(SICI)1097-0061(199807)14:10<943::AID-YEA292>3.0.CO;2-Y.

73. Houseley, J., and Tollervey, D. (2011). Repeat expansion in the budding yeast ribosomal DNA can occur independently of the canonical homologous recombination machinery. Nucleic Acids Res. *39*, 8778–8791. https://doi.org/10.1093/nar/gkr589.

74. Janke, C., Magiera, M.M., Rathfelder, N., Taxis, C., Reber, S., Maekawa, H., Moreno-Borchart, A., Doenges, G., Schwob, E., Schiebel, E., and Knop, M. (2004). A versatile toolbox for PCR-based tagging of yeast genes: new fluorescent proteins, more markers and promoter substitution cassettes. Yeast *21*, 947–962. https://doi.org/10.1002/yea.1142.

75. Schindelin, J., Arganda-Carreras, I., Frise, E., Kaynig, V., Longair, M., Pietzsch, T., Preibisch, S., Rueden, C., Saalfeld, S., Schmid, B., et al. (2012). Fiji - an Open Source platform for biological image analysis. Nat. Methods *9*, 676–682. https://doi.org/10.1038/nmeth.2019.

76. Balakrishnan, R., Park, J., Karra, K., Hitz, B.C., Binkley, G., Hong, E.L., Sullivan, J., Micklem, G., and Cherry, J.M. (2012). YeastMine–an integrated data warehouse for Saccharomyces cerevisiae data as a multipurpose tool-kit. Database *2012*, bar062. https://doi.org/10.1093/database/bar062.

77. Wettenhall, J.M., Simpson, K.M., Satterley, K., and Smyth, G.K. (2006). affylmGUI: a graphical user interface for linear modeling of single channel microarray data. Bioinformatics *22*, 897–899. https://doi.org/10.1093/bioinformatics/btl025.

78. Bolstad, B.M., Irizarry, R.A., Åstrand, M., and Speed, T.P. (2003). A comparison of normalization methods for high density oligonucleotide array data based on

variance and bias. Bioinformatics *19*, 185–193. https://doi.org/10.1093/bioinformatics/19.2.185.

79. Schuhmann, K., Thomas, H., Ackerman, J.M., Nagornov, K.O., Tsybin, Y.O., and Shevchenko, A. (2017). Intensity-Independent Noise Filtering in FT MS and FT MS/MS Spectra for Shotgun Lipidomics. Anal. Chem. *89*, 7046–7052. https://doi.org/10.1021/acs.analchem.7b00794.

80. Herzog, R., Schuhmann, K., Schwudke, D., Sampaio, J.L., Bornstein, S.R., Schroeder, M., and Shevchenko, A. (2012). LipidXplorer: A Software for Consensual Cross-Platform Lipidomics. PLoS One *7*, e29851. https://doi.org/10.1371/journal.pone.0029851.

81. Schuhmann, K., Srzentić, K., Nagornov, K.O., Thomas, H., Gutmann, T., Coskun, Ü., Tsybin, Y.O., and Shevchenko, A. (2017). Monitoring Membrane Lipidome Turnover by Metabolic 15N Labeling and Shotgun Ultra-High-Resolution Orbitrap Fourier Transform Mass Spectrometry. Anal. Chem. *89*, 12857–12865. https://doi.org/10.1021/acs.analchem.7b03437.

82. Güldener, U., Heck, S., Fielder, T., Beinhauer, J., and Hegemann, J.H. (1996). A new efficient gene disruption cassette for repeated use in budding yeast. Nucleic Acids Res. *24*, 2519–2524. https://doi.org/10.1093/nar/24.13.2519.

83. Alberti, S., Gitler, A.D., and Lindquist, S. (2007). A suite of Gateway® cloning vectors for high-throughput genetic analysis in Saccharomyces cerevisiae. Yeast *24*, 913–919. https://doi.org/10.1002/yea.1502.

84. Daniel Gietz, R., and Woods, R.A. (2002). Transformation of yeast by lithium acetate/single-stranded carrier DNA/polyethylene glycol method. In Methods in Enzymology Guide to Yeast Genetics and Molecular and Cell Biology - Part B., C. Guthrie and G.R. Fink, eds. (Academic Press), pp. 87–96. https://doi.org/10.1016/S0076-6879(02)50957-5.

85. Kainz, K., Tadic, J., Zimmermann, A., Pendl, T., Carmona-Gutierrez, D., Ruckenstuhl, C., Eisenberg, T., and Madeo, F. (2017). Chapter Nineteen - Methods to Assess Autophagy and Chronological Aging in Yeast. In Methods in Enzymology Molecular Characterization of Autophagic Responses, Part B., L. Galluzzi, J.M. Bravo-San Pedro, and G. Kroemer, eds. (Academic Press), pp. 367–394. https://doi.org/10.1016/bs.mie.2016.09.086.

86. Eisenberg, T., Carmona-Gutierrez, D., Büttner, S., Tavernarakis, N., and Madeo, F. (2010). Necrosis in yeast. Apoptosis *15*, 257–268. https://doi.org/10.1007/s10495-009-0453-4.

87. Wolinski, H., Bredies, K., and Kohlwein, S.D. (2012). Quantitative imaging of lipid metabolism in yeast: from 4D analysis to high content screens of mutant libraries. Methods Cell Biol. *108*, 345–365. https://doi.org/10.1016/B978-0-12-386487-1.00016-X.

88. Hasek, J. (2006). Yeast fluorescence microscopy. Methods Mol. Biol. *313*, 85–96. https://doi.org/10.1385/1-59259-958-3:085.

89. Pringle, J.R. (1991). Staining of bud scars and other cell wall chitin with Calcofluor. In Methods in Enzymology Guide to Yeast Genetics and Molecular Biology (Academic Press), pp. 732–735. https://doi.org/10.1016/0076-6879(91)94055-H.

90. Vida, T.A., and Emr, S.D. (1995). A new vital stain for visualizing vacuolar membrane dynamics and endocytosis in yeast. J. Cell Biol. *128*, 779–792.

91. Riezman, H., Hase, T., van Loon, A.P., Grivell, L.A., Suda, K., and Schatz, G. (1983). Import of proteins into mitochondria: a 70 kilodalton outer membrane protein with a large carboxy-terminal deletion is still transported to the outer membrane. EMBO J. *2*, 2161–2168.

92. Sales, S., Knittelfelder, O., and Shevchenko, A. (2017). Lipidomics of Human Blood Plasma by High-Resolution Shotgun Mass Spectrometry. Methods Mol. Biol. *1619*, 203–212. https://doi.org/10.1007/978-1-4939-7057-5_16.

93. Sales, S., Graessler, J., Ciucci, S., Al-Atrib, R., Vihervaara, T., Schuhmann, K., Kauhanen, D., Sysi-Aho, M., Bornstein, S.R., Bickle, M., et al. (2016). Gender, Contraceptives and Individual Metabolic Predisposition Shape a Healthy Plasma Lipidome. Sci. Rep. *6*, 27710. https://doi.org/10.1038/srep27710.

94. Schuhmann, K., Almeida, R., Baumert, M., Herzog, R., Bornstein, S.R., and Shevchenko, A. (2012). Shotgun lipidomics on a LTQ Orbitrap mass spectrometer by successive switching between acquisition polarity modes. J. Mass Spectrom. *47*, 96–104. https://doi.org/10.1002/jms.2031.

95. Folch, J., Lees, M., and Stanley, G.H.S. (1957). A Simple Method for the Isolation and Purification of Total Lipides from Animal Tissues. J. Biol. Chem. *226*, 497–509.

96. Schmitz, G., Assmann, G., and Bowyer, D.E. (1984). A quantitative densitometric method for the rapid separation and quantitation of the major tissue and lipoprotein lipids by high-performance thin-layer chromatography: I. Sample preparation, chromatography, and densitometry. J. Chromatogr. *307*, 65–79. https://doi.org/10.1016/S0378-4347(00)84073-6.

97. Schneiter, R., and Daum, G. (2006). Analysis of yeast lipids. Methods Mol. Biol. *313*, 75–84. https://doi.org/10.1385/1-59259-958-3:075.

98. Mangold, H.K. (1961). Thin-layer chromatography of lipids. J. Am. Oil Chem. Soc. *38*, 708–727. https://doi.org/10.1007/BF02633061.

99. Knittelfelder, O.L., and Kohlwein, S.D. (2017). Thin-Layer Chromatography to Separate Phospholipids and Neutral Lipids from Yeast. Cold Spring Harb. Protoc. *2017*. pdb.prot085456. https://doi.org/10.1101/pdb.prot085456.

100. Kolb, D., Pritz, E., Steinecker-Frohnwieser, B., Lohberger, B., Deutsch, A., Kroneis, T., El-Heliebi, A., Dohr, G., Meditz, K., Wagner, K., et al. (2014). Extended Ultrastructural Characterization of Chordoma Cells: The Link to New Therapeutic Options. PLoS One *9*, e114251. https://doi.org/10.1371/journal.pone.0114251.

101. Inaga, S., Katsumoto, T., Tanaka, K., Kameie, T., Nakane, H., and Naguro, T. (2007). Platinum blue as an alternative to uranyl acetate for staining in transmission electron microscopy. Arch. Histol. Cytol. *70*, 43–49. https://doi.org/10.1679/aohc.70.43.

STAR★METHODS

KEY RESOURCES TABLE

REAGENT or RESOURCE	SOURCE	IDENTIFIER
Antibodies		
α-Phospho-p44/42 MAPK	cell signaling	#9101
α-Yeast act1 Goat monoclonal antibody	John Cooper	N/A
α-GAPDH	Life Technologies	MA515738; RRID: AB_10977387
α-VDAC/porin	Abcam	ab110326; RRID: AB_10865182
IRDye goat anti-mouse	Licor	#926–68070; RRID: AB_10956588
IRDye goat anti-rabbit	Licor	#926-68071; RRID: AB_10956166
Bacterial and virus strains		
pYX122-mtGFP	B. Westermann[71]	pCG44
pRS426-SLT2-GFP	Matthias Peter[35]	PPR A75
pAG418-POR1	This study	YPR B06
pDONR221-*POR1*	DNASU	FLH201444.01X
pFA6a-KanMX6	Addgene.org [72]	#39296; PPR C31
pFA6a-Ura3	Addgene.org [73]	#61924; PPR C29
pYM27	EUROSCARF[74]	YPR B35
Chemicals, peptides, and recombinant proteins		
Cercosporamide (CSA)	Sigma-Aldrich	SML0172
Calcofluor white (CFW)	Sigma-Aldrich	910090
Phalloidin-Tetramethylrhodamine B-Isothiocyanate	Sigma-Aldrich	P1951
SynaptoRed™ C2 (equivalent to FM4-64)	Biotum	BOT-70021
Rhodamine B hexylester perchlorate	Molecular Probes	Y-7530
Bodipy 493/503	Sigma-Aldrich	#490389
Autodot	Abcepta	# SM1000a
Critical commercial assays		
RNAeasy kit	Qiagen	#74004
Yeast 2.0 GeneChip array	Affymetrix	#900553
Deposited data		
Raw and analyzed data	This paper	Mendeley Data: https://doi.org/10.17632/bgkscw9ns9.1
Microarray	This paper	Mendeley Data: https://doi.org/10.17632/bgkscw9ns9.1
Shotgun lipidomics	This paper	Mendeley Data: https://doi.org/10.17632/bgkscw9ns9.1
HPTLC lipidomics	This paper	Mendeley Data: https://doi.org/10.17632/bgkscw9ns9.1
Experimental models: Organisms/strains		
S. cerevisiae: Strain background: BY4742 Matα *ura3*-52 *his3*Δ200 *leu2*-3,112 *lys2*-801 *ade2*-101 *COF1::LEU2*	Pekka Lappalainen[25]	YPR K43
cof1-5 COF1::LEU2	Pekka Lappalainen[25]	YPR K44
*por1*Δ	This paper	YPR K45
cof1-5 por1Δ	This paper	YPR K46
*lro1*Δ	This paper	YPR K62
cof1-5 lro1Δ	This paper	YPR K47

(*Continued on next page*)

Continued

REAGENT or RESOURCE	SOURCE	IDENTIFIER
*dga1*Δ	This paper	YPR K63
cof1-5 dga1Δ	This paper	YPR K48
*lro1Δ dga1*Δ	This paper	YPR K64
*cof1-5 lro1Δ dga1*Δ	This paper	YPR K49
slt2Δ	This paper	YPR T29
cof1-5 slt2Δ	This paper	YPRT31
Wt SLT2-EGFP	This paper	YPR T12
cof1-5 SLT2-EGFP	This paper	YPR T15
S. cerevisiae: Strain background: BY4741 MATa *ACT1::HIS3 his3*D200 *tub2*-101 *ura3*-52 *leu2*-3, 112	David Drubin[32]	YPR K50
MATa *act1*-159::*HIS3 his3*D200 *tub2*-101 *ura3*-52 *leu2*-3, 112	David Drubin[32]	YPR K51
Oligonucleotides		
LRO1_fw:CCATTACAAAAGGTTCTCTAC CAACGAATTCGGCGACAATCGAGTAA AAACAGCTGAAGCTTCGTACGC	This paper	N/A
LRO1_rev:TTCGCTCTTTGAAATAATACA CGGATGGATAGTGAGTCAATGTCGGT CATGCATAGGCCACTAGTGGATCTG	This paper	N/A
DGA1_fw:TACATATACATAAGGAAACGC AGAGGCATACAGTTTGAACAGTCACAT AACAGCTGAAGCTTCGTACGC	This paper	N/A
DGA1_rev:AAAATCCTTATTTATTCTAACA TATTTTGTGTTTTCCAATGAATTCATTAG CATAGGCCACTAGTGGATCTG	This paper	N/A
POR1-S1: CCAACACGAAACAGCCAAGCG TACCCAAAGCAAAAATCAAACCAACCTC TCAACACGTACGCTGCAGGTCGAC	This paper	A80
POR1-S2: AAGAACGAGCACATATATGGTA TATAGTGAACATATATATATTAGATATATA CGTATCGATGAATTCGAGCTCG	This paper	A81
SLT2-S1: CTATCAAAATAGTAGAAATAATT GAAGGGCGTGTATAACAATTCTGGGAGA TGCGTACGCTGCAGGTCGAC	This paper	B40
SLT2-S2: CTTACATCTATGGTGATTCTATA CTTCCCCGGTTACTTATAGTTTTTTGTCC TAATCGATGAATTCGAGCTCG	This paper	B41
SLT2-S3: GCTTCTAGACCTTGAAAAAGAG CTGGAGTTTGGATTAGATAGAAAATATTT TCGTACGCTGCAGGTCGAC	This paper	B42
PKC1-S2: CCGCTTAGATGTTTTATATAAAA TTAAATAAATCATGGCATGACCTTTTCTTC AATCGATGAATTCGAGCTCG	This paper	B45
PKC1-S3: GCCAGCAAGAAGAGTTTAGAGG ATTTTCCTTTATGCCAGATGATTTGGATTTA CGTACGCTGCAGGTCGAC	This paper	B46
Software and algorithms		
Fiji (ImageJ)	https://imagej.nih.gov/ij/ [75]	N/A

(*Continued on next page*)

Continued

REAGENT or RESOURCE	SOURCE	IDENTIFIER
GraphPad Prism 8.4.3	www.graphpad.com	N/A
R (3.1.0)	www.R-project.org	N/A
Slim Mapper	https://www.yeastgenome.org/goSlimMapper	N/A
Yeastmine	https://yeastmine.yeastgenome.org/yeastmine/begin.do [76]	N/A
Bioconductor plugin affylmgui	Wettenhall et al.[77]	N/A
Robust Multi-Array Average (RMA) algorithm	Bolstad et al.[78]	N/A
PeakStrainer	https://git.mpi-cbg.de/labShevchenko/PeakStrainer/wikis/home [79]	N/A
LipidXplorer software	Herzog et al.[80]	N/A
in-house-developed script	Schuhmann et al.[81]	N/A
Other		
Resource website for yeast genetics SGD	https://www.yeastgenome.org/ [33]	N/A

RESOURCE AVAILABILITY

Lead contact

Further information and requests for resources and reagents should be directed to and will be fulfilled by the lead contact Patrick Rockenfeller (Patrick.rockenfeller@uni-wh.de) and Campbell Gourlay (C.W.Gourlay@Kent.ac.uk).

Materials availability

Plasmids and yeast strains generated in this study are available upon request.

Data and code availability

- Microarray data, original western blot images, lipidomics data and Prism files have been deposited at Mendeley and are publicly available as of the date of publication. Mendeley Data: https://doi.org/10.17632/bgkscw9ns9.1. Microscopy data reported in this paper will be shared by the lead contact upon request.
- This paper does not report original code.
- Any additional information required to reanalyse the data reported in this paper is available from the lead contact upon request.

EXPERIMENTAL MODEL AND SUBJECT DETAILS

All experiments (except Figure 3) were carried out using the wildtype (Matα *ura3*-52 *his3*Δ200 *leu2*-3,112 *lys2*-801 *ade2*-101 *COF1*::*LEU2*) and *cof1-5* mutant (Matα *ura3*-52 *his3*Δ200 *leu2*-3,112 *lys2*-801 *ade2*-101 *cof1-5*::*LEU2*) *S. cerevisiae* strains as generated and described by Lappalainen et al.[15] Additional gene-knock outs in these two strains for *LRO1* and *DGA1* were generated using the Cre-LoxP system with the KanMX marker for selection[82] using the primers as listed in the key resources table. The *lro1Δ dga1Δ* double knock out was generated based on the *dga1*::kanMX single knock out strain using the pFA6a-Ura3-cassette[73] for the additional LRO1 knock out. POR1-, and SLT2-gene knock outs were generated according to the protocols and primer design of Janke et al.[74] using the pFA6a-KanMX6-cassette.[72] See key resources table for primer sequences.

For the experiments shown in Figure 3 the *act1-159* mutant (MATa *act1*-159::*HIS3 his3*D200 *tub2*-101 *ura3*-52 *leu2*-3, 112) which harbours the V159N mutation and has reduced actin dynamics was used together with its corresponding wildtype control strain (MATa *ACT1*::*HIS3 his3*D200 *tub2*-101 *ura3*-52 *leu2*-3, 112).[32]

Plasmids were propagated in *E. coli* K12 DH5α (see key resources table for details). *POR1* was cloned into pAG416GPD CEN URA by gateway-cloning[83] using pDONR221-*POR1* as a donor-plasmid. pYX122-mtGFP was obtained from Benedikt Westermann.[71] The *SLT2*-GFP expression plasmid was obtained from Matthias Peter.

Slt2-EGFP as shown in Figure 5A and Pkc1-EGFP as shown in Figure 5J was expressed under control of their endogenous promoters at their original loci. These strains were generated by PCR and homologous recombination according to established protocols[74] using the plasmid pYM27 and primers as listed in the KRT, except for the experiment shown in Figures 5F–5I, where Slt2-GFP was expressed from a plasmid pRS426-SLT2-GFP.[35] Transformation of yeast cells with plasmids or linear DNA for homologous recombination was performed using the lithium acetate method.[84] At least three different clones were tested to rule out clonogenic variations.

All experiments (except for ageing experiments as shown in Figures 4G–4J) were carried out in yeast peptone medium with glucose (YPD). YPD medium contains 1% yeast extract (BD), 2% peptone (BD), and 2% glucose. Synthetic complete medium with glucose without Uracil (SCD-Ura), was only used when selection was required for strain construction or to maintain selection for plasmids. SC medium contains 0.17% yeast nitrogen base (Difco), 0.5% $(NH_4)_2SO_4$, and 30 mg/L of all amino acids (except 80 mg/L histidine and 200 mg/L leucine), 320 mg/L uracil, 30 mg/L adenine, and 2% glucose. All media were prepared with ultrapure water (MilliQ) and subsequently autoclaved (20 min, 121°C, 110 kPa). Amino acid mixtures and glucose were sterilised separately as 10× stocks and added after autoclaving. All yeast cultures were inoculated from a stationary overnight culture to an OD_{600} = 0.1 and then grown at 30°C and 145 rpm shaking for indicated time points.

METHOD DETAILS

Growth assays

Strains were inoculated from stationary overnight cultures to an OD_{600} of 0.1 in 24-well plates (Sarstedt, 1 ml total volume per well) in two or three independent experiments, each containing at least three biological replicates. The plate was automatically measured for 24–48 h using a BMG LabTech SPECTROstar^{Nano} plate reader with double orbital shaking at 400 rpm and 30°C, with OD_{600} measurements every 30 min. Growth curves were plotted in GraphPad Prism.

Analysis of cell viability, density and diameter

Propidium iodide (PI) staining was used to determine loss of membrane integrity.[85,86] Cells were harvested in 96-well plates at indicated time points and resuspended in 250 µL of 100 µg/L PI in PBS, and incubated in the dark for 10 min at room temperature. After incubation, cells were washed once with 250 µL PBS and analysed via flow cytometry (Beckmann Coulter Cytoflex). A total of 30,000 cells per strain and condition were measured and analysed with CytExpert software. For calcofluor white (CFW) stress experiment in Figure 4E, wt and *cof1-5* cells were grown overnight and inoculated to an OD_{600} of 0.1, then grown at 30°C. After 22 h of growth, cells were subjected to either 100 µM cercosporamide, 200 µM CFW or both, and allowed to grow for further 26 h. CFW stress at 200 µM as shown in Figures 4F, S4A, and S4B was carried out at exponential growth phase (6 h after inoculation to an OD_{600} of 0.1) and PI was detected 18 hours after stress. For chronological ageing analysis cultures were inoculated to an OD_{600} of 0.1 in SCD medium as mentioned above with additional supplementation of 90 mg/ L lysine (+3x), 10 g/ L myo-inositol (55µM), and 97.8 mg/ L adenine. Samples were measured at indicated days of ageing by clonogenic survival plating and PI staining to determine viability.

For clonogenic survival plating serial dilutions of the main cultures were used to measure cell densities using a CASY cell counter essentially as described before.[12] As an adaptation to former protocols the serial dilutions of all strains were made using ddH_2O containing 10 mM EDTA. The addition of EDTA avoided cell aggregation, which is a characteristic of *cof1-5* cells. Without EDTA treatment reliable estimation of living cells by counting of colony forming units (CFU) was impossible.

Mean cell diameters were determined based on measurement with a CASY cell counter, which calculates mean cell size based on electric currency shifts which are due to the cells acting as electric isolators in conducting salt solution. For these measurements the complex cell mixtures containing cells at all replicative

stages were used, which includes single mother cells, bud-containing mother cells and single daughter cells.

Fluorescence microscopy

S. cerevisiae strains were inoculated to an OD_{600} = 0.1 from overnight cultures in YPD medium and harvested at 6h after inoculuation for analysis at exponential growth phase or 24h for analysis at stationary phase. Cells were immobilised on microscopy slides containing 2% agarose.[87] Fluorescence was detected using a Nikon Eclipse Ni-U fluorescence microscope with a Hamamatsu Orca-Spark C11440-36U monochromatic camera and Nikon Intensilight C-HGFI illumination system. Fluorescence images were captured and saved as z-stacks in a range of 5 μm with 200 nm steps using NIS-Elements BR 4.13.05 64-bit with N-dimensional acquisition. Deconvolution and colocalisation analysis was performed with Huygens essential 21.10 software. Further processing such as maximum intensity z-projection, brightness/contrast adaptation, scale bar inclusion, colour merging was performed in Fiji/ ImageJ.[75]

Actin was stained using Phalloidin-Tetramethylrhodamine B-Isothiocyanate (Sigma, P1951) essentially as described before.[88] In brief, approximately 10^7 cells were harvested and fixed with 3.7 % formaldehyde. Cells were washed in PEM buffer (100 mM PIPES, 5 mM EGTA, 5 mM $MgCl_2$, pH 6.9) and stained with 50 μg/ml final concentration of Phalloidin-TRITC in PEM buffer with 25 % methanol. After washing cells were resuspended in PEM buffer containing DAPI at a final concentration of 2.5 μg/ml and mounted on agarose slides for microscopy.

Nuclear staining of live cells in Figure 5A was performed using Hoechst (bisbenzimide H 33342).

Cell wall staining for chitin exposure was performed using calcofluor white fluorescent brightener (Sigma, 910090) at a final concentration of 100 μg/ml.[89]

The vacuole morphology was visualised by staining with SynaptoRed(TM) C2 (equivalent to FM4-64; Biotum BOT-70021) as described before.[90]

Rhodamine B hexylester perchlorate (Molecular Probes, Y-7530) was used at a final concentration of 100 nM to stain functional mitochondria. Pearson colocalisation coefficients for Slt2-GFP colocalization with Rhodamine B hexylester signal were determined in Huyghens essential 21.10 using the colocalization analyzer wizard with Gaussian minimum estimation.

Lipid droplets were stained with Bodipy 493/503 or autodot. Bodipy was detected in the FITC channel whereas autodot was detected in the DAPI channel. Quantification of lipid droplets was performed after threshold setting with the "analyze particle" tool and total cell numbers were counted with the "cell counter" plugin.

RNA isolation and microarray

Total RNA was prepared from wild type and *act1-159* log phase cells from biological triplicate cultures using a Qiagen RNAeasy kit including an on-column DNAse digestion step according to the manufacturer's instructions. Following reverse transcription reactions the cDNA template was hybridised to an Affymetrix Yeast 2.0 GeneChip array. Data was quality controlled and normalised using the Bioconductor plugin, affylmgui.[77] To reduce background noise we used the Robust Multi-Array Average (RMA) algorithm.[78] The affylmGUI package was run using R (version 3.1.0) to generate volcano plots. A significance threshold value for 95% odds of differential expression was chosen, which corresponds to a B statistic of 2.94 and above. We then sorted the significant data into groups for processing using Gene Ontology (GO) Slim Mapper and Yeastmine[76] analysis tools from SGD.[33]

Immunoblotting

For Western blot analysis, cell equivalents of an OD_{600} of 3 were harvested at 24 h after inoculation, and cell extracts were obtained from chemical lysis as described in.[91] Proteins were collected by centrifugation and resuspended in 75 μL 1× loading buffer (125 mM Tris-HCl, adjusted to pH 6.8; 20% glycerol; 3% SDS; 2% DTT; 0.1% bromophenol blue), and heated to 95°C for 10 min. Samples were centrifuged at 13,000 rpm for 12 s and 10 μL or 15 μL of the supernatant was used for standard SDS-PAGE. Immunoblotting followed standard procedures, with transfer of proteins to a 0.45 μm nitrocellulose membrane and probing with

antibodies against phospho-Slt2 (Phospho-p44/42 MAPK, cell signaling, #9101, 1:1000), actin (α-Yeast act1 Goat monoclonal antibody, a kind gift from Prof. John Cooper, Washington University, 1:2000), (glyceraldehyde-3-phosphate dehydrogenase (GAPDH, Life Technologies, MA515738, 1:5000), or VDAC/porin (Abcam, ab110326, 1:5000). As secondary antibodies, we used IRDye goat anti-mouse (Licor, 926–68070, 1:20,000) or IRDye goat anti-rabbit (Licor, 928-40028, 1:20,000) as listed in the key resources table. Signals were recorded with Odyssey Glx, with automatically determined exposure times. Quantitative analysis of western blots was performed using image studio software.

Lipid extraction and quantification by shotgun mass spectrometry

Yeast cultures were inoculated from stationary overnight cultures in YPD to fresh YPD medium to an OD_{600} of 0.1. In total, 2 OD_{600} units were harvested after 24 h and homogenised with 0.5 mm zirconia beads in a cooled tissue lyser for 2 × 10 min at 30 Hz in 300 μL IPA. The whole homogenate was evaporated in a vacuum desiccator to complete dryness. Lipid extraction was performed according to.[92–94] In brief, 700 μL internal standard mix in 10:3 MTBE/MeOH was added to each sample and vortexed for 1 h at 4°C. After the addition of 140 μL H_2O, samples were vortexed for another 15 min. Phase separation was induced by centrifugation at 13,400 rpm for 15 min. The organic phase was transferred to a glass vial and evaporated. Samples were reconstituted in 300 μL 1:2 MeOH/$CHCl_3$. For lipidome, 5 μL of sample were diluted with 95 μL 4:2:1 IPA/MeOH/CHCl3 + 7.5 mM ammonium formate.

Mass spectrometric analysis was performed on a Q Exactive instrument (Thermo Fisher Scientific, Bremen, DE) equipped with a robotic nanoflow ion source TriVersa NanoMate (Advion BioSciences, Ithaca, NY, USA) using nanoelectrospray chips with a diameter of 4.1 μm. The ion source was controlled by the Chipsoft 8.3.1 software (Advion BioSciences). Ionisation voltage was +0.96 kV in the positive and −0.96 kV in the negative mode; back pressure was set at 1.25 psi in both modes. Samples were analysed by polarity switching.[94] The temperature of the ion transfer capillary was 200°C; S-lens RF level was set to 50%. Each sample was analysed for 18 min. FT-MS spectra were acquired within the range of m/z 400–1000 from 0 min to 0.2 min in the positive mode, and within the range of m/z 350–1200 from 6.2 min to 6.4 min in the negative mode at a mass resolution of R m/z 200 = 140,000, automated gain control (AGC) of 3 × 10^6, and with a maximal injection time of 3000 ms. Ergosterol was determined by parallel reaction monitoring (PRM) FT-MS/MS between 0.2 and 1.7 min. For FT-MS/MS, micro-scans were set to 1, isolation window to 0.8 Da, normalised collision energy to 12.5%, AGC to 5 × 10^4, and maximum injection time to 3000 ms. t-SIM in positive (1.7 to 6 min) and negative (6.4 to 18 min) mode was acquired with R @ m/z 200 = 140,000; automated gain control of 5 × 10^4; maximum injection time of 650 ms; isolation window of 20 Th; and scan range of m/z 400 to 1000 in positive and m/z 350 to 1200 in negative mode, respectively. The inclusion list of masses targeted in t-SIM analyses started at m/z 355 in negative and m/z 405 in positive ion mode, and other masses were computed by adding 10 Th increment (i.e., m/z 355, 365, 375, …) up to m/z 1005 in positive mode and up to m/z 1205 in negative mode. All acquired spectra were filtered by PeakStrainer (https://git.mpi-cbg.de/labShevchenko/PeakStrainer/wikis/home)[79] and stitched together by an in-house-developed script.[81] Lipids were identified by LipidXplorer software.[80] Molecular fragmentation query language (MFQL) queries were compiled for ergosterol, ergosterol esters, PC, LPC, PE, LPE, PI, LPI, PA, LPA, PG, LPG, PS, LPS, TG, DG, IPC, MIP2C, and MIPC lipid classes. The identification relied on accurately determined intact lipid masses (mass accuracy better than 5 ppm) and a signal-to-noise threshold higher than 3. Lipids were quantified by comparing the isotopically corrected abundances of their molecular ions with the abundances of internal standards of the same lipid class. Ergosterol, as well as ergosterol esters, were normalised to the internal cholesterol and internal CE standard, respectively.

Lipid extraction and quantification by thin-layer chromatography

Yeast cultures were inoculated from stationary overnight cultures in YPD to fresh YPD medium to an OD_{600} of 0.1. In total, 80 OD600 units were harvested at 24 h after inoculation. Total lipids were extracted with chloroform/methanol 2:1 (*v/v*) according to Folch et al.[95] Cholesterylformate (Sigma, S448532) was added to each sample before extraction as an internal standard. The organic phase was dried under a stream of nitrogen and dissolved in 1 mL of chloroform/methanol (2:1, *v/v*). For neutral lipid separation a total of 40 μL of lipid extracts was sprayed on HPTLC silica gel 60 plates, 20 x 10 cm (Merck, 1.05641.001) using a CAMAG automatic TLC sampler (ATS4), whereas for phospholipid analysis only 20 μL were applied. Lipid separation was performed using a CAMAG automatic developing chamber (ADC2). Neutral lipids were separated with n-hexane, n-heptane, diethylether, acetic acid (63/18.5/18.5/1 v/v) as mobile phase,[96] whereas phospholipid separation was carried out using $CHCl_3$/MeOH/water (32.5:12.5:2) mixture as mobile phase.[97–99]

HPTLC plates were derivatized with 0.01 % primuline applied in a CAMAG derivatizer followed by mild heating to 40°C for 2 minutes on a CAMAG TLC plate heater 3. Developed HPTLC plates were imaged using a CAMAG TLC visualizer 2 with VisionCATS software. Since peak separation of PI and PS was not ideal in all samples we conducted an additional derivatisation step with ninhydrin spray reagent (Sigma Aldrich, N1286), which only stains phospholipids containing free amino groups and thus allows quantification of PS without PI. HPTLC bands were processed into chromatograms and quantified by polynomial regression of standard curves calculated from the applied standards. For phospholipids the standard contained l-α-phosphatidylinositol (840044P), phosphatidylcholine (16:0-18:1; 850457P), phosphatidylethanolamine (16:0-18:1; 850757P), phosphatidylserine (18:1-18:1; 840034P), cardiolipin (18:1-18:1; 710335P), phosphatidic acid (16:0-18:1; 840101P) each at 500 ng/μl all purchased individually from Sigma Aldrich. As a neutral lipid standard we either used a 1:10 dilution of the nonpolar lipid mixture B from Matreya (#1130) which is an equal component mix of cholesteryl-oleate, methyloleate, triolein, oleic acid, and cholesterol (each at 5 μg/μl) additionally supplemented with diacylglycerol (16:0-18:1; Sigma 800815O) or a custom-made neutral lipid standard consisting of a mix of cholesteryl-oleate (700269P), cholesterylformate (S448532), triolein (870110O), diacylglycerol (16:0-18:1; 800815O), oleic acid (O1008) all purchased individually from Sigma Aldrich, and ergosterol from Thermofisher Scientific (117810050) each at 500 ng/μl. The standards were applied at increasing quantities from 250 ng to 15 μg absolute mass.

Electron microscopy high pressure freezing with a Leica EM HPM 100 and freeze substitution

Yeast strains were inoculated from a stationary overnight culture in YPD to an OD_{600} of 0.1. Cells were grown in YPD media and harvested at stationary phase after 24 h of growth and immediately subjected to high pressure freezing. Cell peletts were loaded and frozen using 2000 bar under liquid nitrogen conditions within milliseconds. Freezing was followed by freeze substitution in acetone by adding 2 % osmium tetroxide (OsO_4) and 0.2 % uranyl acetate (UAc) at temperatures below −70°C. After substitution, the samples were embedded in TAAB (Agar Scientific, Essex,GB) epoxy resin.[100] High pressure frozen yeast cells were sectioned (70 nm) with a UC7 Ultramicrotome (Leica Microsystems, Vienna, Austria) and stained with lead citrate for 5 min and platinum blue[101] for 15 min. Images were taken at 120 kV with a Tecnai G2 FEI (Thermo Fisher Scientific) microscope equipped with an Ultrascan 1000 CCD Camera (Gatan). Measurement of cell wall thickness on electron micrographs was performed in ImageJ using the measure tool. For each strain condition at least 117 measurements of the inner and outer cell wall at equally distributed loci around the cells were performed.

QUANTIFICATION AND STATISTICAL ANALYSIS

Statistical analyses were calculated in Graphpad Prism 8. Information on tests for significance is given in each figure. Error bars indicate standard error of the mean (SEM) and asterisks in the figures indicate significant differences, *p<0.05, **p<0.01, ***p<0.001, ****p<0.0001.